Journal of Nanobiotechnology

RESEARCH

Open Access

Cyclic cell-penetrating peptide-engineered ceria nanoparticles for non-invasive alleviation of ultraviolet radiation-induced cataract

Luyang Jiang[1,2†], Jinxia Liu[1†], Silong Chen[1†], Wenyu Cui[1†], Jiarui Guo[1], Xiaoyu Cheng[1], Yingying Zheng[1], Wenxin Yang[1], Zicai Pan[1], Yao Wang[1], Mary Zhao[3], Haijie Han[1], Ke Yao[1*] and Yibo Yu[1*]

Abstract

Oxidative stress, which results from the accumulation of free radicals, plays a substantial role in cataract formation. Antioxidants have shown promise in mitigating or even preventing this process. However, delivering antioxidants noninvasively to the anterior segment of the eye has been a significant challenge. In this study, we developed ceria nanoparticles modified with cyclic cell-penetrating peptides to overcome the obstruction of the dense corneal barrier on topical drug delivery. Our results demonstrated that modified ceria nanoparticles with cell-penetrating peptides (CPPs) facilitate the opening of tight junctions in human corneal epithelial cells. This characteristic considerably enhances the trans-corneal transport of nanoparticles and improves cellular uptake efficiency, while also contributing to their intracellular enrichment toward mitochondria. Further experiments confirmed that the modified ceria nanoparticles effectively counteracted ferroptosis induced by oxidative stress in lens epithelial cells both in vitro and in vivo, substantially reducing cataract formation. The successful development of ceria nanoparticles modified with cyclic cell-penetrating peptides (cCPPs) opens new avenues for research in cataract prevention and treatment. Additionally, the modified ceria nanoparticles could serve as a noninvasive drug delivery system, which holds remarkable potential for advancing drug delivery in diseases affecting the anterior segment of the eye.

Keywords Oxidative stress, Ferroptosis, Cataracts, Antioxidants, Ceria nanoparticles, Cyclic cell-penetrating peptides

†Luyang Jiang, Jinxia Liu, Silong Chen and Wenyu Cui contributed equally to this work.

*Correspondence:
Ke Yao
xlren@zju.edu.cn
Yibo Yu
yuyibo@zju.edu.cn
Full list of author information is available at the end of the article

Graphical Abstract

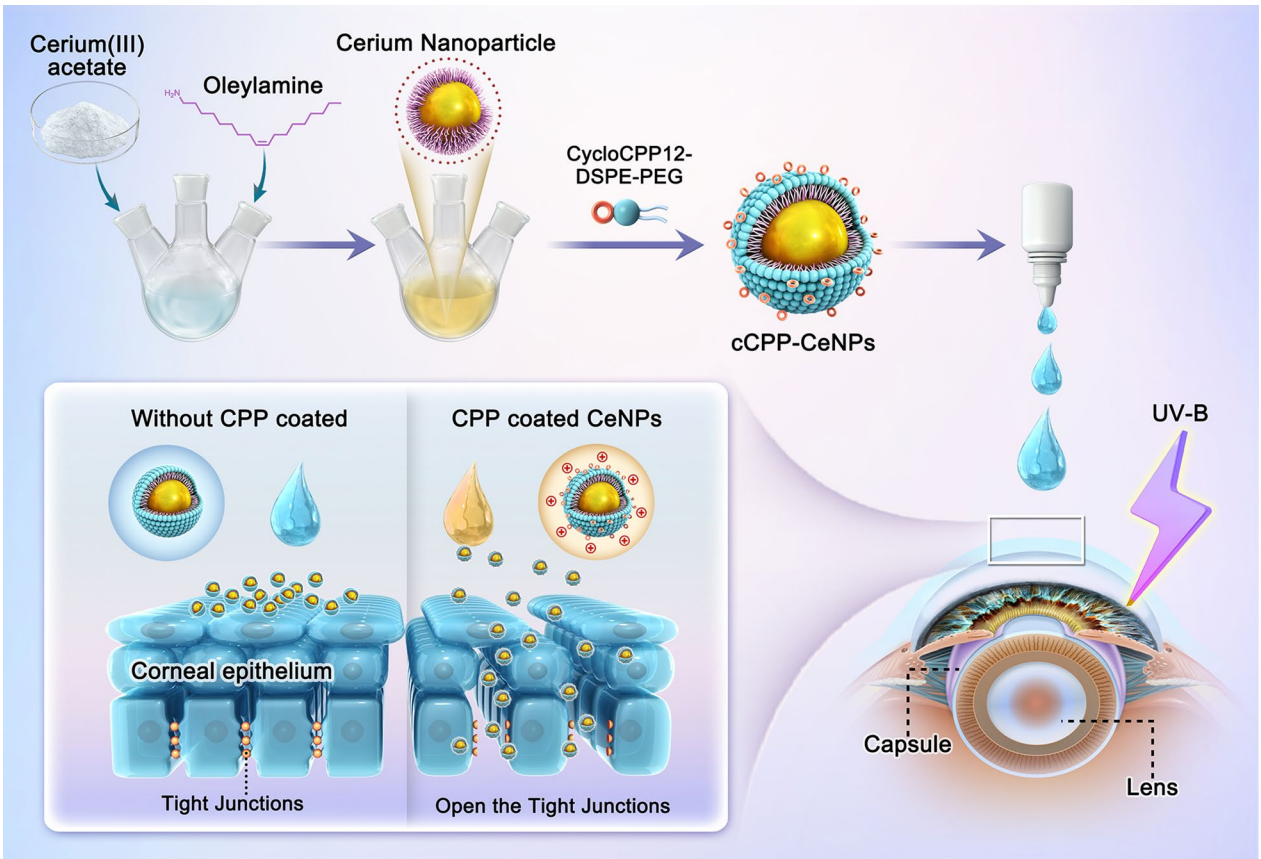

Introduction

Cataracts are the leading cause of blindness worldwide, which affects an estimated 83.5 million individuals aged 50 years and older, severely impairing their quality of life [1]. While cataract surgery is widely recognized as a cost-effective intervention in developed areas, people in remote or economically disadvantaged areas still lack timely access to this treatment, therefore missing the optimal therapeutic window [2]. Consequently, researchers worldwide have endeavored non-surgical approaches to decelerate or halt the progression of cataracts for decades in order to reduce cataract-induced blindness. The occurrence and development of age-related cataracts is a slow and multifactorial process, during which oxidative stress was identified as a crucial risk factor [3–5]. Oxidative stress refers to a condition characterized by an excess of oxidants relative to antioxidants, which can potentially lead to harm or damage [6, 7]. Various external stimuli, such as radiation, toxins, and inflammation, can lead to the generation of reactive oxygen species (ROS) within cells. When these stimuli persist or their intensity suddenly escalates, cells may fail to eliminate the excessive ROS promptly. This disruption of cellular homeostasis can further lead to cell death. Therefore, when the body is unable to escape from such pathological insults, timely intervention to assist cells in clearing ROS is crucial. Breaking this harmful cycle not only prevents further damage but also facilitates tissue repair and promotes the recovery of organ function [8, 9]. Over the past three decades, researchers have conducted extensive screenings and investigations to assess the anti-oxidative effectiveness of natural and synthetic antioxidants. Numerous antioxidants have shown encouraging outcomes in treating preclinical models of cataracts. However, their application has predominantly been limited for the systemic administration routes via oral, intraperitoneal, or intravenous in experimental animals [10–13]. The main obstacle in delivering antioxidants to the anterior segment through topical application lies in the unique structure of the ocular surface, including the dense corneal epithelial

barrier and the rapid turnover of the tear film [14, 15]. Thus, achieving efficient noninvasive delivery to the ocular anterior segment area remains a challenge [16, 17].

Ferroptosis, an emerging research focus in recent years, has garnered significant attention across nearly all biomedical fields [18–20]. In particular, ferroptosis is recognized as an important pathophysiological process involved in various diseases, including neurodegenerative disorders, stroke, traumatic brain injury, ischemia–reperfusion injuries, liver fibrosis, and acute kidney injury [21, 22]. An expanding body of research has identified numerous genes and pathways associated with ferroptosis. Among them, pathways that influence glutathione peroxidase 4 (GPX4) activity, redox-active iron levels, and glutathione (GSH) homeostasis are essential for the regulation of cell death mediated by the oxidation of polyunsaturated fatty acid (PUFA)-containing phospholipids [23]. In detail, GPX4 is currently regarded as the only enzyme capable of detoxifying hydroperoxides of PUFA-containing phospholipids (PL) [24, 25]. Although research on ferroptosis in lens diseases is still in its infancy, existing evidence have indicated that aged human lenses and cataractous lenses exhibit hallmarks of ferroptosis, including disrupted redox homeostasis, reduced GSH levels, impaired GPX activity, elevated redox-active iron content, and increased lipid peroxidation [26, 27]. These changes align with the fundamental criteria defining ferroptosis. Thus, exploring therapeutic strategies aimed at preventing or treating cataracts by targeting and inhibiting ferroptosis holds significant potential. Such approaches could pave the way for novel interventions to preserve lens transparency and prevent vision loss associated with cataracts.

The initial permeability barrier for drugs to penetrate through the dense corneal barrier to the anterior segment is the dynamic, rapid-regenerating tear film [28–30]. Within the tear film, the mucus layer plays a role as the greatest barrier, characterized by negatively charged glycans and hydrophobic pore structure [31, 32]. Thus, it is plausible to hypothesize that particles with a positive charge on the surface can effectively adhere to the tear film [33]. After penetrating through the tear film, what lies ahead is the dense corneal barrier, consisting of alternating hydrophilic and hydrophobic layers between different strata, making it nearly impossible for most drug molecules to passively diffuse and reach the anterior chamber [17, 34]. The outer multi-layered cornea epithelium is hydrophobic and features tight junctions between cells, forming a dense barrier that primarily hinders the diffusion of hydrophilic drugs through paracellular channels [35]. In contrast, the stroma is a hydrophilic fibrous layer that restricts the penetration of hydrophobic molecules through transcellular pathways. Therefore, the molecular size and hydrophobicity/hydrophilicity of drugs are key factors influencing their permeability through the cornea [31].

Ceria nanoparticles (CeNPs), with a size of less than 5 nm, possess a unique surface composition that includes both trivalent (Ce^{3+}) and tetravalent (Ce^{4+}) states, resulting in the presence of abundant oxygen vacancies within their lattice structure [36–39]. This characteristic enables CeNPs to exhibit antioxidant activity through electron transfer between cerium(III) and cerium(IV) [40–43]. Moreover, due to the inherent memory function of the lattice structure and their capacity to exchange electrons with other ions, these ultrafine ceria nanoparticles can readily restore their redox activity [39, 42, 44, 45]. This property repeatedly allows them to eliminate reactive oxygen species (ROS), showcasing their remarkable self-regeneration properties. The auto-regenerative multienzyme activity of CeNPs, including superoxide dismutase [46, 47] and catalase [48], has attracted significant attention among researchers in the field of biomedical science in recent years. The potential therapeutic effects of CeNPs have been demonstrated in various oxidative stress-related disease models, including neurodegenerative diseases [44], cardiac protection applications [49], skin injuries hair loss [50, 51], and eye disorders, such as age-related macular degeneration [52, 53], dry eye [54], chemical burn [55], and acute glaucoma [56].

In recent years, research on nanotechnology-based drug delivery has made significant advancements. Among these, ceria nanoparticles (CeNPs) have emerged as a promising solution for addressing the long-standing challenges of drug delivery to the anterior segment of the eye. Their exceptional versatility, precise control over particle properties, and direct surface modification capabilities make CeNPs highly adaptable for ophthalmic applications. Given the challenges associated with drug delivery to the ocular surface or intraocular tissues, recent years have seen several successful strategies, with the application of cell-penetrating peptides (CPPs) standing out as particularly noteworthy [31, 57–59]. Surface modification of nanomaterials with CPPs significantly enhances their bioavailability, whether applied to the ocular surface [60] or administered via intravitreal injection [61]. In this study, we employed amphiphilic cyclic cell-penetrating peptides (cCPPs) [62] and 1,2-distearoyl-sn-glycero-3-phosphoethanolamine-N-[methoxy(polyethyleneglycol)−2000] ($DSPE\text{-}mPEG_{2000}$) to surface-modify hydrophilic CeNPs. As a result (Fig. 1), we successfully synthesized nanoparticles with a highly positive surface charge and excellent medium dispersion performance, referred to as cCPP-CeNPs. We demonstrated that modified cCPPs on the surface of nanoparticles greatly enhance their ability to penetrate the corneal barrier and

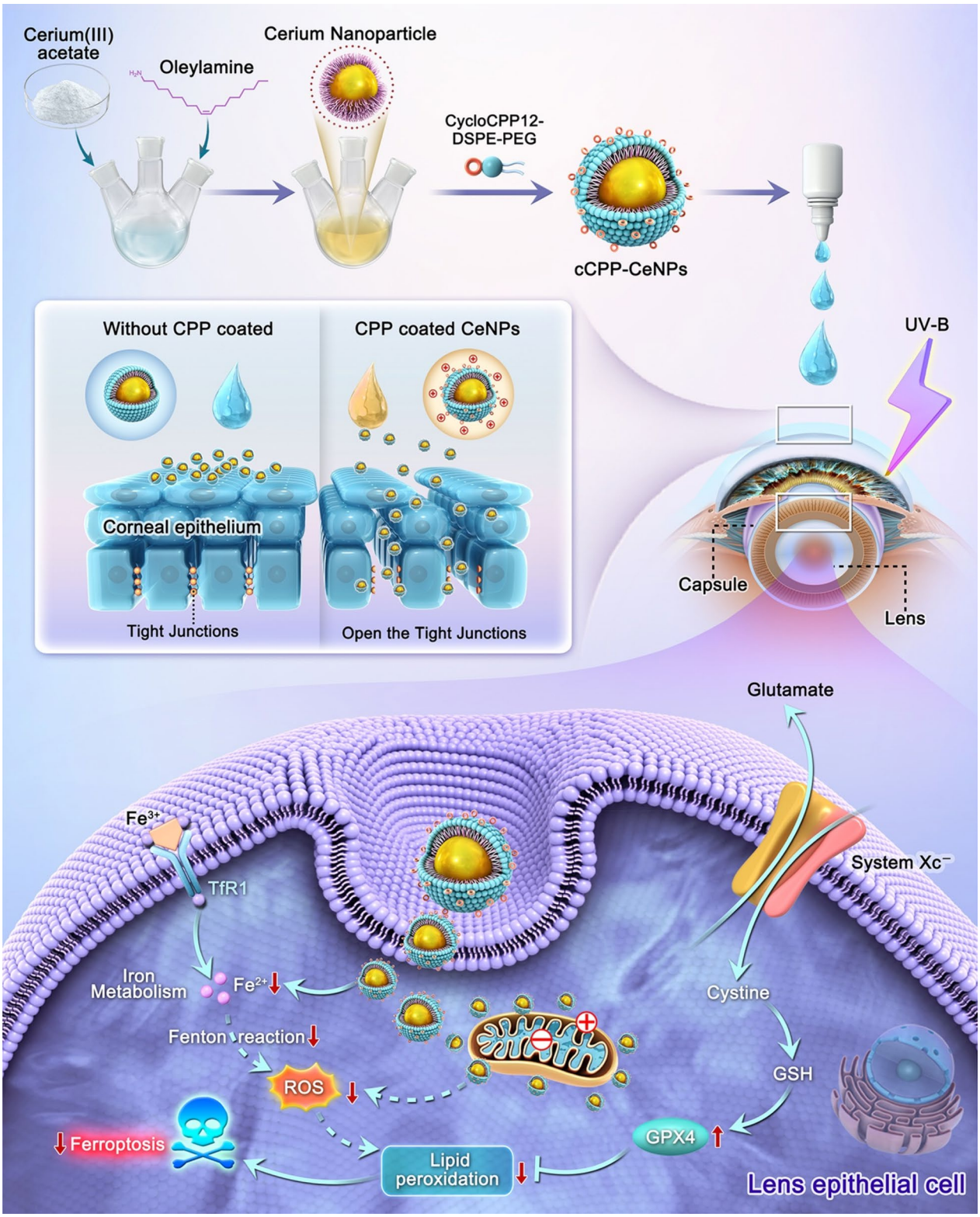

Fig. 1 Schematic diagram showing the synthesis process and mechanism of cCPP-CeNPs for alleviating cataracts

accumulate within lens epithelial cells. Subsequently, using both in vitro cell lines and in vivo mouse models of ultraviolet radiation-induced cataracts, we found that the cCPP-CeNPs effectively cleared ROS in lens epithelial cells and mitigated cataract formation through inhibition of cell ferroptosis. This study highlights the potential of cell-penetrating peptides (CPPs), particularly cCPPs-engineered ceria nanoparticles, in noninvasive drug delivery to the anterior segment, paving the way for novel avenues of future research.

Methods

Materials and animals

Cerium acetate (99.99%) and xylene (98.5%) were obtained from Aladdin Industrial, Inc. (Shanghai, China). Oleylamine (70%) was purchased from Sigma-Aldrich Co. (St. Louis, MO). DSPE-mPEG$_{2000}$ was obtained from A.V.T. (Shanghai) Pharmaceutical Co. Ltd. Cyclo[Ff-(2-Nal)-RrRrQC-DSPE-mPEG$_{2000}$] (Remark: f is D-Phe, r is D-Arg), Ff-(2-Nal)-RrRrQC-DSPE-mPEG$_{2000}$) (Remark: f is D-Phe, r is D-Arg), and FITC-DSPE-mPEG$_{2000}$ were purchased from ChinaPeptides Co. Ltd. (QYAOBIO). FITC was acquired from Shanghai Yuanye Biotechnology Co., Ltd. Tissue-Tek OCT Compound was obtained from Sakura Finetek USA. Ultrapure water (18.2 MΩ·cm) was provided by a Milli-Q filtration instrument.

Synthesis of CeNPs

CeNPs were synthesized through hydrolytic sol–gel reactions [44, 63]. In brief, 0.43 g of cerium(III) acetate (1 mmol) and 3.25 g of oleylamine (12 mmol) were dissolved in 15 mL of xylene. The mixture solution was stirred vigorously for 12 h at room temperature and then heated to 90 °C at a rate of 2 °C/min under an argon atmosphere. Deionized water (1 mL) was rapidly injected into the heated solution to initiate the sol–gel reaction, evidenced by the color change from purple to cloudy yellow. The reaction mixture was maintained at 90 °C for 3 h until it became transparent and subsequently cooled to room temperature. Ceria NPs were precipitated by adding 100 mL of acetone, collected by centrifugation, and then resuspended in chloroform to achieve a final concentration of 10 mg/mL. The resulting purified CeNPs were readily dispersed in chloroform for storage and use.

Synthesis of three sets of water-dispersive ceria NPs and FITC-conjugated ceria NPs

To synthesize biocompatible CeNPs, these were coated with DSPE-PEG co-polymer using a combination of the film hydration method [64]. Briefly afterwwards, 30 mg of DSPE-mPEG$_{2000}$ (1.1×10^{-2} mmol) was dissolved in 5.0 mL of chloroform and then mixed with chloroform containing 10 mg of CeNPs. The solution was evaporated using a rotary evaporator and dried under vacuum at room temperature for 90 min. Ten milliliters of deionized water were added to the flask, followed by sonication. The resulting transparent, light-yellow suspension was filtered using a syringe filter with a 0.2 μm pore size. To remove free DSPE-mPEG$_{2000,}$ the PEG-CeNPs were thoroughly purified by sequentially treating the nanoparticles with high-speed ultracentrifugation at 450,000 g for 2 h and filtration using an Amicon centrifugal filter with a 30 kDa cutoff molecular weight. The purified PEG-CeNPs were stored in double distilled water (ddH_2O) at 4 °C.

Water-dispersive lCPP-CeNPs and cCPP-CeNPs were obtained using the same procedures as for the preparation of water-dispersive PEG-CeNPs, except that a mixture of linearCPP/CyclicCPP-conjugated DSPE-PEG$_{2000}$ and DSPE-PEG$_{2000}$ was used in a 1:3 ratio of linearCPP/CyclicCPP-DSPE-PEG$_{2000}$ to DSPE-PEG$_{2000}$.

To produce FITC-conjugated ceria or linearCPP/CyclicCPP-ceria nanoparticles, FITC-conjugated DSPE-PEG$_{2000}$ was used together with either DSPE-PEG$_{2000}$ or a mixture of linearCPP/CyclicCPP-conjugated DSPE-PEG$_{2000}$ with DSPE-PEG$_{2000}$ at a ratio of 1 to 50 during the water-transfer of ceria nanoparticles.

Characterization of three types of CeNPs

Hydrodynamic diameters and zeta potentials for the PEG-CeNPs, lCPP-CeNPs, and cCPP-CeNPs were measured using dynamic light scattering with a Zetasizer Nano-ZS system (Malvern Instruments, Inc., Worcestershire, UK) and disposable folded capillary cells. The morphology of nanoparticles was characterized by the Hitachi HT7700 TEM (Hitachi, Tokyo, Japan) and high-resolution transmission electron microscope (HR-TEM) (Talos F200X G2, Thermo Fisher Scientific). XRD patterns were recorded using RIGAKU SmartLab SE. XPS spectra were performed using Thermo Scientific K-Alpha. Inductively coupled plasma mass spectrometry (Agilent 7700 Series ICP-MS) was employed to measure the retained concentrations of cerium in solution or in the aqueous humor of C57BL/6 J mice's eyes.

Electron paramagnetic resonance experiments

5,5-Dimethyl-1-Pyrroline-N-Oxide (DMPO) was obtained from J&K Scientific Ltd., Beijing, China. Iron(II) sulfate heptahydrate was sourced from Sigma-Aldrich, Milwaukee, WI, USA. Stock solutions were prepared using deionized water (Milli-Q, Millipore Synergy UV water purification system, Merck Millipore, Billerica, MA, USA), 0.88 M DMPO, 1.0 mM Fe(II) sulfate, and 10 mM hydrogen peroxide. Stock solutions of three types of CeNPs were initially prepared at a concentration of 0.5 mM.

For spin trapping experiments, samples were prepared as follows: 2.84 μL of DMPO stock solution was added to 12.5 μL of aqueous iron sulfate solution. Subsequently, 12.5 μL of hydrogen peroxide stock solution was added to initiate the reaction, marking the start of timing. After incubating the mixture for 5 min to form hydroxyl radical adducts, 25 μL of the sample under study (or water in control experiments) was added, mixed, and the liquid was aspirated into the capillary for the electron paramagnetic resonance (EPR) experiment.

SOD activity assay

The superoxide scavenging activity was assessed using a SOD assay kit from Beyotime Biotechnology. Initially, three types of CeNPs were diluted in 200 μL of WST-1 (water-soluble tetrazolium salt; 2-(4-iodophenyl)−3-(4-nitrophenyl)−5-(2,4-disulfophenyl)−2H-tetrazolium, monosodium salt) solution at cerium concentrations of 0.1 and 1.0 mM and added in triplicate to each well. The SOD coupling reactions commenced with the addition of 20 μL of xanthine oxidase solution, followed by incubation at 37 °C for 20 min. The absorbance at 450 nm, proportional to SOD activity, was measured using an iMark Microplate Absorbance Reader (Bio-Rad Laboratories, Inc. USA). An SOD activity of 50 U/mL was defined as the enzyme activity that inhibits the reduction reaction of WST-1 with the superoxide anion by 50% in experiments quantifying SOD-mimetic activity. Three repeated sets of measurements were performed.

Cell culture and cytotoxicity detection

The human lens epithelial cell line (HLEB3) was cultured in Dulbecco's Modified Eagle's Medium (DMEM) with 10% fetal bovine serum (FBS) and maintained in a 37 °C incubator with 5% CO_2. For cytotoxicity detection, HLEB3 cells were seeded in 96-well plates (1×10^4 cells/well) and cultured for 24 h. CeNPs were diluted in cell culture medium to equal ceria concentration and incubated with HLEB3 cells for 2 h. Subsequently, the cell culture medium was replaced with phenol red-free medium (containing 10% FBS) for exposure to UVB radiation at varying concentrations (0, 20, 40, 60, 80, and 100 mJ/cm^2). After a further 24-h incubation, cell viability was measured using a Cell Counting Kit-8 (CCK-8) assay according to the manufacturer's instructions. All experiments were performed in triplicates independently.

ROS detection

HLEB3 cells were seeded in 24-well plates (5×10^4 cells/well) and pretreated with PEG-CeNPs, lCPP-CeNPs, and cCPP-CeNPs for 2 h before UVB stimulation. The ROS content was detected using a Dichloro-dihydrofluorescein diacetate (DCFH-DA) kit according to the manufacturer's instructions. Following the different interventions, HLEB3 cells were incubated with DCFH-DA dilution for 30 min, after which the fluorescence was observed and captured using fluorescence microscopy.

Ferrorange staining

FerroOrange (Dojindo Laboratories, Japan) was used to detect the iron content in HLEB3 cells. The cells were seeded in 24-well plates (5×10^4 cells/well) and pretreated with PEG-CeNPs, lCPP-CeNPs, and cCPP-CeNPs for 2 h before UVB stimulation; PBS treatment served as the control group. Following administration, HLEB3 cells were stained with a FerroOrange dilution (diluted in DMSO, 1 μmol/L) for an additional 30 min of incubation. Images were observed and captured using fluorescence microscopy. The experiments were conducted in triplicate.

JC-1 staining

Mitochondrial membrane potential (ΔΨm) was evaluated using a JC-1 kit. HLEB3 cells were seeded in 24-well plates and subjected to various interventions. Subsequently, the cells were stained with JC-1 staining solution and incubated for an additional 20 min at 37 °C. Cell images were observed and captured using confocal microscopy. At high mitochondrial membrane potential, JC-1 aggregated in the mitochondrial matrix, forming J-aggregates that produced red fluorescence. Conversely, at low mitochondrial membrane potential, JC-1 did not accumulate in the mitochondria's matrix and remained a monomer, resulting in green fluorescence.

Mito-FerroGreen staining

Mito-FerroGreen is a novel fluorescent probe for detecting ferrous ions in mitochondria. In this experiment, HLEB3 cells were seeded in 24-well plates and subjected to various treatments. After medium removal, HLEB3 cells were washed three times with serum-free medium. Then, the Mito-FerroGreen working solution (5 mol/L, containing 200 nmol/L MitoTracker Red) was added, and the cells were incubated for 30 min at 37 °C in a 5% CO_2 incubator. Subsequently, the supernatant was removed, and the cells were washed three times with serum-free medium. Erastin, the activator, was then added and the incubation continued for another 1 h. Finally, images were observed and captured using confocal microscopy.

Cellular uptake and mitochondria-targeting ability

To investigate the cellular uptake ability of our CeNPs, we added free-FITC, PEG-CeNPs, lCPP-CeNPs, or cCPP-CeNPs modified FITC (equal concentration, 500 μM) to HLEB3 plates (24 well, 5×10^4 cells per well) and incubated for 2 h. The cellular uptake ability was assessed

by the fluorescence intensity of FITC observed under microscopy. Subsequently, after removing the FITC medium, we added MitoTracker Red solution (200 nM) to the plates and cultured them for an additional 30 min at 37 °C in the incubator. Colocalization analysis of MitoTracker and CeNPs modified FITC was conducted using Image J.

Preparation and imaging of the eyeball tissue using TEM

To assess the alteration of tight junctions between corneal epithelial cells, C57BL/6 J mice's eyes underwent topical administration with PBS, PEG-CeNPs, lCPP-CeNPs, or cCPP-CeNPs eyedrops (1 h per time, four times). After 4 h, the mice were sacrificed, and their corneas were harvested immediately and fixed for TEM imaging. To determine changes in mitochondria of LECs, HLEB3 cells and C57BL/6 J mice were pretreated with CeNPs, followed by UVB radiation (60 mJ/cm^2 for HLEB3 cells, 3.6 kJ/m^2 for mice), and corresponding samples were collected. The samples were then fixed overnight in glutaraldehyde solution.

For fixing samples, samples mentioned above were then fixed in 1% osmium tetroxide for another 2 h. Each fixation step was followed by a 15-min rinse in PBS (pH 7.0) three times to remove remaining fixatives. The samples were then dehydrated in a graded ethanol series (50%, 70%, 80%, 90%, and 95%) and pure acetone for 20 min each at room temperature. For permeabilization, the samples were treated successively with a mixture of Spurr embedding agent and acetone (volume ratio 1:1) for 1 h, a mixture (volume ratio 3:1) for 3 h, and pure Spurr embedding agent overnight. Afterward, the samples were embedded and cut into slices (70 nm thickness). The images were observed using a Hitachi H-7650 transmission electron microscope.

Immunofluorescence staining

To identify the expression of ferroptosis-related markers in mouse LECs, C57BL/6 J mice were randomly divided into five groups: Control, UVB + PBS, UVB + PEG-CeNPs, UVB + lCPP-CeNPs, and UVB + cCPP-CeNPs. After euthanization, the mice's eyeballs were fixed in 4% paraformaldehyde solution overnight. For evaluating the distribution of tight junctions in corneal epithelial cells, mice were randomly divided into four groups (PBS, PEG-CeNPs, lCPP-CeNPs, or cCPP-CeNPs). Corneas were collected and fixed in 4% paraformaldehyde solution overnight. The following day, samples were placed in an OCT agent post-intervention and transferred to − 80 °C. The samples were then subjected to frozen sections. Subsequently, OCT agent was washed off using PBS, and the samples were permeabilized with 0.25% Triton X-100 at room temperature for 20 min, blocked with 5% bovine serum albumin at room temperature for 1 h, and incubated with the primary antibodies: anti-ASCL4 (1:200, ABclonal, A6826, USA), anti-GPX4 (1:200, ABclonal, A13309, USA), anti-xCT (1:500, Affinity, DF12509, USA), anti-TfR1 (1:200, ABclonal, A5865, USA), and anti-ZO-1 (1:200, Abcam, ab68477, USA) at 4 °C overnight. On the second day, the sections were incubated with a secondary antibody (CoraLite594-conjugated Goat Anti-Rabbit IgG (H + L), SA00013-4, Proteintech, USA) at room temperature for 1 h, and then the slices were observed and captured using confocal microscopy.

Lipid peroxidation

The lipid peroxidation of HLEB3 cells was investigated using the Lipid Peroxidation Probe-BDP$^{581/591}$ C11 (Dojindo Laboratories, Japan). HLEB3 cells were seeded in 24-well plates (5×10^4 cells/well) and subjected to specific treatments. Subsequently, BDP$^{581/591}$ C11 working solution was added to the cells and incubated for 30 min in a 37 °C incubator with 5% CO_2. After removing the solution and washing the cells with FBS-free medium, images were captured using fluorescence microscopy. The fluorescent probe emits red fluorescence under normal conditions, and the fluorescence changes from red to green during lipid peroxidation. Thus, the formation of lipid peroxides can be detected with high sensitivity by the fluorescence intensity of red and green.

H&E staining

The collected tissues (including eyeballs, heart, liver, spleen, lung, and kidney) were fixed with 4% paraformaldehyde, embedded in paraffin, and sectioned. Subsequently, tissue paraffin sections, 5 μm thick, were stained with H&E and observed and imaged using optical microscopy.

Western blotting

To determine the expression of ferroptosis-related proteins, HLEB3 cells were divided into six groups: Control, UVB, UVB + PBS, UVB + PEG-CeNPs, UVB + lCPP-CeNPs, and UVB + cCPP-CeNPs. The total proteins of cells were lysed using Radio-immunoprecipitation assay (RIPA) lysis plus 1% protease inhibitors (PMSF), and the protein concentration was measured by bicinchoninic acid (BCA) assay. Proteins (10 μg) were subjected to sodium dodecyl sulfate–polyacrylamide gel electrophoresis (SDS-PAGE) gel electrophoresis, and polyvinylidene fluoride or polyvinylidene difluoride (PVDF) membranes were incubated with the following primary antibodies: anti-ASCL4 (1:1000, ABclonal, A6826, USA), anti-GPX4 (1:1000, ABclonal, A13309, USA), anti-xCT (1:2000, Affinity, DF12509, USA), and anti-TfR1 (1:1000,

ABclonal, A5865, USA). The ImageJ software was used to quantify the intensity of each target gene.

Experimental animals

We conducted UVB irradiation-induced cataract studies using adult C57BL/6 J female mice, aged 6–8 weeks (purchased from the Experimental Animal Center of Hangzhou Medical College). The mice, weighing approximately 20 g upon arrival, were fed ad libitum and kept under standard conditions with a 12 h light/dark cycle. They were acclimatized and habituated to the laboratory for 3 days prior to the experiments. Prior to experiments, all mice were examined using a slit lamp (66 Vision Co., Suzhou, China). Only mice without anomalies in the anterior segment of the eye (cornea, anterior chamber, iris, or lens) were included in the studies. The Institutional Animal Care and Use Committee approved the use of animals for this study. The mice were maintained and treated in accordance with the Association for Research in Vision and Ophthalmology Statement for the Use of Animals in Ophthalmic and Vision Research.

Experimental grouping and UV exposure

C57BL/6 female mice, aged 6 weeks and weighing 18–20 g, were acclimatized for three days before being randomly allocated into six groups for eyedrop treatment. PBS (untreated), PEG-CeNPs, lCPP-CeNPs (3.0 mg/mL), low-concentration cCPP-CeNPs (1.0 mg/mL), high-concentration cCPP-CeNPs (3.0 mg/mL), and pirenoxine sodium eye drops groups were used in the experiments. The administration of eye drops started one day before exposure to UV light. Eye drops (20 μL each) were applied four times a day at intervals of 3 h and continued until 7 days after exposure to UVB.

Mice were anesthetized by intraperitoneal injection of sodium pentobarbital (45 mg/kg body weight). Five minutes after the injection, 1% tropicamide was administered to both eyes to induce pupil dilation. The unexposed eye on the contralateral side was shielded throughout the exposure period for comparison. The left eye of the mouse was subjected to UVB light emitted from a Philips ultraviolet lamp (peak wavelength: 311 nm) for 10 min at a constant distance of 12 cm between the ultraviolet lamp and the mouse cornea. Here, 0.3% sodium hyaluronate eye drops were utilized to prevent corneal dryness during irradiation. Post-UVB exposure, carbomer ophthalmic gel was applied to the eyes to avert exposure to keratitis. Subsequently, the mice were allowed to return to their original cages. UVB light intensity was measured using a UV detector (UVB ultraviolet irradiation meter, Beijing Normal University Optoelectronic Instrument Factory, Beijing, China). We monitored the instantaneous illumination on the corneal plane at 0.6 mW/cm^2, which resulted in a final irradiation dose of approximately 3.6 kJ/m^2.

Lens morphologic examination

The anterior segment underwent examination using a slit lamp (66 Vision Co., Suzhou, China) before UV exposure. Morphological changes in the cornea and lens were monitored via slit lamp microscopy at various time points after exposure. However, UV-induced corneal cloudiness hindered the slit lamp examination of the lens, necessitating enucleation of the lenses. These were then examined and photographed under a dissecting microscope (Leica stereo microscopes) using dark field illumination, ensuring meticulous recording of all morphological changes.

Statistical analysis

Quantitative data were displayed as mean ± standard deviation (SD) and were analyzed using SPSS version 25.0 software. Significance between two groups was assessed through a two-tailed *t*-test, while the Kruskal–Wallis test determined significance when parametric tests were unsuitable for the data. One-way ANOVA with Bonferroni correction established significance among multiple groups. A p-value <0.05 was defined as significant. Graphs were plotted using GraphPad Prism 8 software.

Results

Synthesis and characterization of CeNPs

Hydrophobic uniform-sized CeNPs with a diameter of approximately 3 nm were synthesized using reverse micelle method [44, 65, 66], as evidenced by the transmission electron microscopy (TEM) images (Fig. 2A). After surface modification, the ceria nanoparticles maintained a pure and typical fluorite cubic structure, as demonstrated by selected area electron diffraction (SAED) patterns (Fig. 2B) and X-ray diffraction (XRD) analysis (Fig. 2C). The X-ray photoelectron spectroscopy (XPS) analysis (Fig. 2D) indicated the coexistence of Ce^{3+} and Ce^{4+} on the surface of CeNPs, which provided the structural basis for the enzymatic reactions [67]. We quantified the surface concentrations of cerium(III) (peaks at 885.0 and 903.5 eV) and cerium(IV) (peaks at 882.1, 888.1, 898.0, 900.9, 906.4, and 916.4 eV), and found that the slightly yellow ceria nanoparticles contained a cerium(III) content of approximately 43.62% (Fig. 2D). Subsequently, to enhance water dispersibility and biocompatibility, CeNPs were coated with either DSPE-PEG_{2000}, referred to as PEG-CeNPs or linearCPPs/cyclicCPPs-conjugated-1,2-distearoyl-sn-glycero-3-phosphoethanolamine-N-[amino(polyethyleneglycol)−2000] (DSPE-mPEG-linearCPPs or DSPE-mPEG-cyclicCPPs), referred to as lCPP-CeNPs, and cCPP-CeNPs, respectively. DSPE-mPEG-linearCPPs

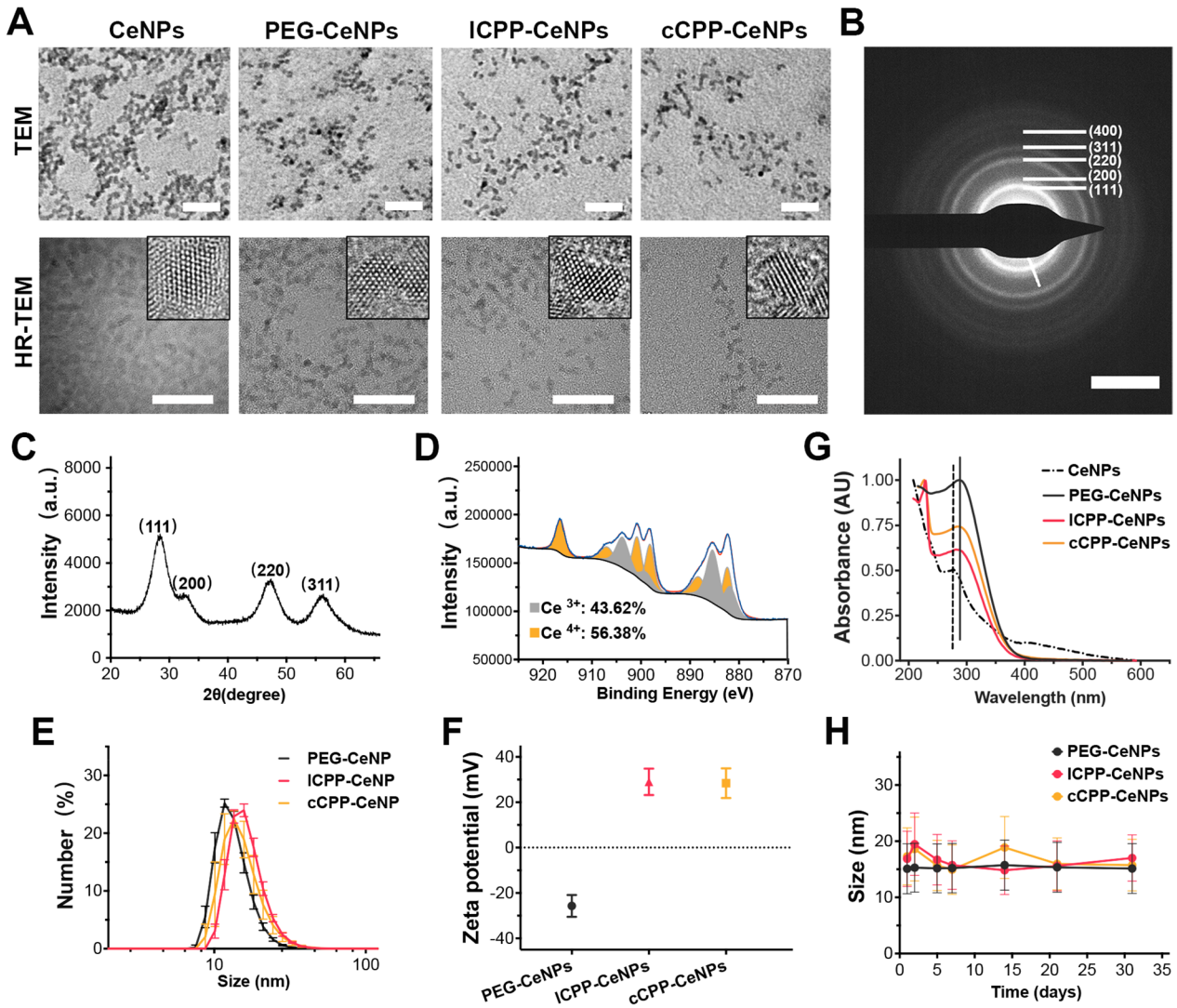

Fig. 2 Illustration of ceria nanoparticles and their morphology, structure, size, surface charges, and stability. **A** Representative TEM and HR-TEM images of CeNPs dispersed in chloroform, PEG-CeNPs, lCPP-CeNPs and cCPP-CeNPs dispersed in water (scale bar: 20 nm). **B** The SAED pattern (right panel) of CeNPs dispersed in chloroform (scale bar: 5 nm). **C** XRD analysis of CeNPs. **D** XPS spectra of CeNPs. **E** Hydrodynamic diameters of PEG-CeNPs, lCPP-CeNPs and cCPP-CeNPs. **F** ζ-potentials of PEG-CeNPs, lCPP-CeNPs and cCPP-CeNPs. **G** UV–Vis spectrum of ceria nanoparticles before (dotted line) and after (solid line) surface modification. **H** Size changes of PEG-CeNPs, lCPP-CeNPs and cCPP-CeNPs in artificial tears over 30 days

and DSPE-mPEG-cyclicCPPs were obtained through the conjugation of the cysteine residue of linear[Ff-(2-Nal)-RrRrQC] (where f is d-phenylalanine, r is d-arginine, 2-Nal is l-2-naphthylalanine) or cyclo[Ff-(2-Nal)-RrRrQC] with the maleimide group in DSPE-PEG-Mal. The purified products (DSPE-PEG-linearCPPs and DSPE-PEG-cyclicCPPs) were quality-checked by the matrix assisted laser desorption ionization (MALDI) TOF mass spectrum. The results (Fig. S1 and S2) showed that the molecular weight of DSPE-PEG-linearCPPs or DSPE-PEG-cyclicCPPs was approximately 4200 g/mol. Specifically, the molecular weight of linearCPPs or cyclicCPPs was around 1350 g/mol each. Moreover, the molecular weight of DSPE-PEG_{2000} is about 2900 g/mol. These results suggested that the cell-penetrating peptides were successfully conjugated to DSPE-PEG_{2000}. TEM analysis demonstrated that the three groups of nanoparticles (PEG-CeNPs, lCPP-CeNPs, and cCPP-CeNPs) all presented a core diameter of approximately 3 nm (Fig. 2A). The hydrodynamic diameters of PEG-CeNPs, lCPP-CeNPs, and cCPP-CeNPs were approximately 15 nm, and the zeta potential underwent a transition from

−25.7 to +29 mV, respectively (Fig. 2E and F). These changes in size and surface potential confirmed the successful conjugation of lCPPs or cCPPs onto the CeNPs. Figure 2G depicted the UV–vis absorption spectrum of ceria nanoparticles before and after surface modification. The absorption spectrum exhibited intense peaks in the range of 280–300 nm, which are recognized as the characteristic peaks of CeNPs. After surface modification, the characteristic peaks of the nanoparticles displayed a subtle redshift, as illustrated by the dotted line in Fig. 2G. The hydrodynamic diameters of ceria nanoparticles in artificial tears (Fig. 2H), ultrapure water (Fig. S3), and phosphate-buffered saline (PBS) (Fig. S4) were monitored over a span of 30 days. During this period, the hydrodynamic diameters in all three different media remained relatively constant, indicating the excellent colloidal stability of these ceria nanoparticles under physiological conditions.

Auto-regeneration feature and ROS scavenging performance of ceria nanoparticles in vitro

To assess the auto-regenerative properties of the ceria nanoparticles, 0.02 M H_2O_2 was added to 10 mM stock solution of the nanoparticles (Fig. 3A). Upon addition,

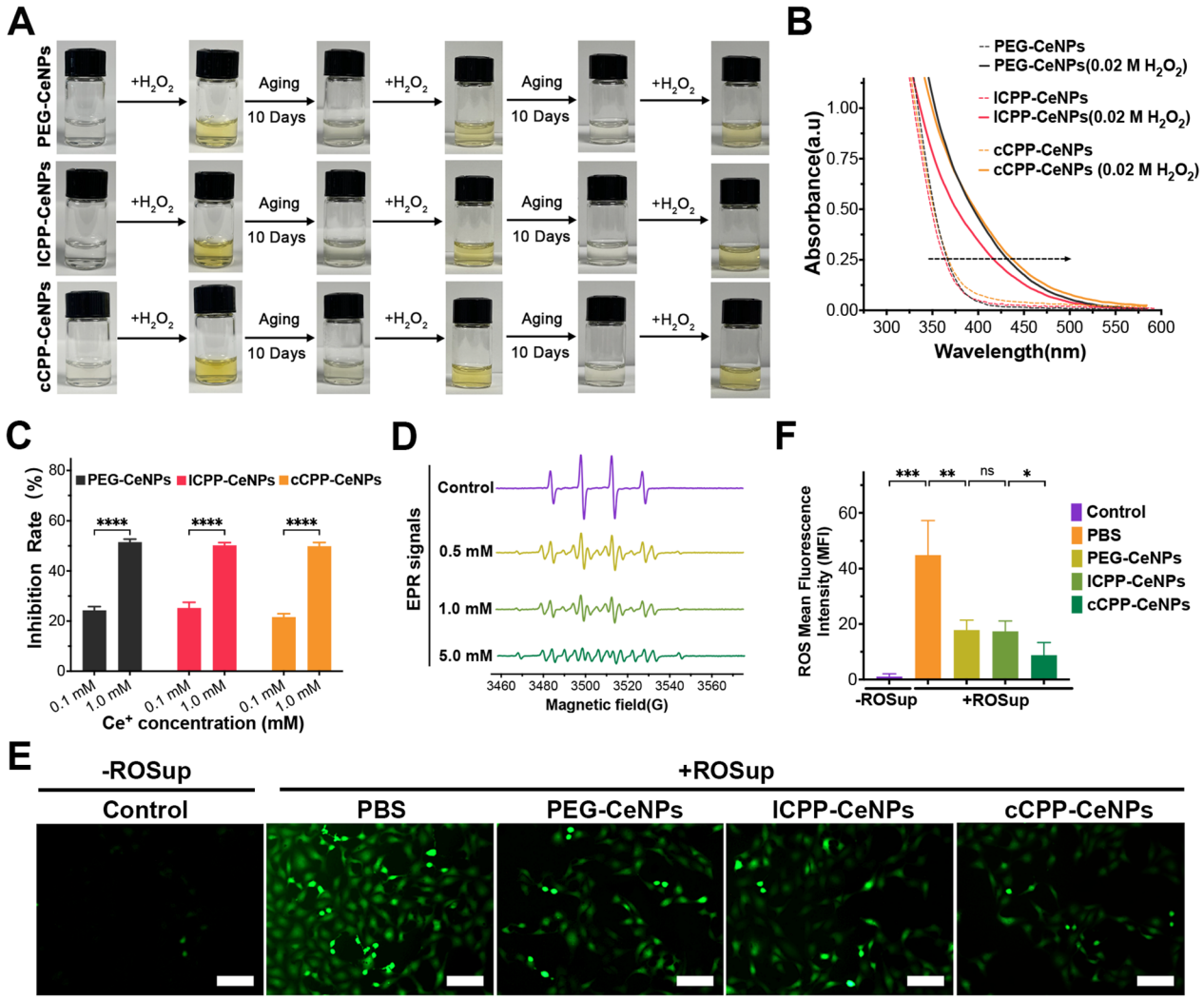

Fig. 3 ROS scavenging performance and auto-regeneration feature of ceria nanoparticles. **A** Color changes of CeNPs upon adding H_2O_2 and subsequent aging. **B** The UV–Vis spectrum depicting H_2O_2 quenching of the water-soluble PEG-CeNPs, lCPP-CeNPs, and cCPP-CeNPs. The band exhibited a red shift from the control (dotted line) to the as-reacted solution (solid line) upon H_2O_2 adding. **C** SOD-mimetic activities of PEG-CeNPs, lCPP-CeNPs, and cCPP-CeNPs. **D** Experimental X-band (9.867 GHz) ESR spectra of aqueous solutions of Control, 0.5 mM cCPP-CeNPs, 1.0 mM cCPP-CeNPs, and 5.0 mM cCPP-CeNPs. **E** and **F** Representative ROS staining images (**E**) of lens epithelial cells in the presence of Rosup and ceria nanoparticles and statistics of relative mean fluorescence intensity (**F**) (scale bar: 100 μm). In all histograms, data is presented as the mean ± SD (Standard Deviation) ($n = 3$). *$p < 0.05$, **$p < 0.01$, ***$p < 0.001$, ****$p < 0.0001$; ns, no significance

the solution rapidly changed to a dark yellow color on the first day. After ten days, the samples returned to a colorless state. Subsequently, the oxidation process reoccurred in the same sample on the 10 th day with an additional 0.02 M H_2O_2. The surface modification of lCPP/cCPP showed no effects on their auto-regeneration properties. All three surface-modified nanoparticles were reusable and could continue to scavenge free radicals. Corresponding to the color change reaction, the characteristic absorption peak underwent a redshift following the addition of H_2O_2 (represented by the solid line) compared to the control (depicted by the dashed line) in the UV–Vis spectrum (Fig. 3B). In addition, as shown by XPS analysis (Fig. S5), most of Ce^{3+} in the nanoparticles were oxidized to Ce^{4+}. To evaluate the catalytic activities of ceria nanoparticles in terms of superoxide dismutase (SOD)-mimic activity and hydroxyl radical antioxidant capacity (HORAC) (Fig. 3C and D), the elimination of superoxide anions and hydroxyl radicals (·OH) was examined. The CeNPs exhibited SOD-mimic activity in a concentration-dependent manner (Fig. 3C). Furthermore, electron spin resonance (ESR) spectra proved that CeNPs efficiently scavenged the ·OH radicals generated by the Fenton reaction (Fig. 3D, S6, and S7). These findings underscore the excellent ROS-scavenging capabilities of the CeNPs. Finally, when we simultaneously employed nanoparticles and Rosup to treat cells, and then assessed the ROS levels within the cells, we observed a notable reduction in ROS levels after nanoparticles treatment (Fig. 3E). The nanoparticles demonstrated remarkable ROS removal effects, with the most significant impact observed in the cCPP-CeNPs group (Fig. 3F). These outcomes serve as a solid foundation for our subsequent experiments.

Mechanisms of topical ophthalmic delivery of CeNPs

To evaluate the in vivo penetrating capability of CeNPs, we detected the distribution of fluorescein isothiocyanate (FITC)-modified PEG-CeNPs, lCPP-CeNPs, and cCPP-CeNPs in the entire mice eyeball. As shown in Fig. 4A, FITC was only observed on the surface of the cornea in mice treated with free-FITC. In contrast, mice treated with PEG-CeNPs displayed notable fluorescence extending from the corneal epithelium to the corneal endothelium. Moreover, weak fluorescent signals were detected in the anterior capsule of the lens in mice treated with lCPP-CeNPs, whereas stronger fluorescent signals were observed after cCPP-CeNPs administration, indicating the superior penetrating ability of cCPP-CeNPs. Then, to elucidate the mechanism underlying the enhanced permeation of cCPP-CeNPs, we conducted trans-endocytosis experiments. As shown in Figure S8, we first treated HCECs seeded on coverslip A with FITC-labeled CeNPs for 24 h, and then this coverslip was co-cultured with a second coverslip (coverslip B) in fresh culture medium for another 24 h. Distinct green fluorescence on the coverslip B indicated that a certain amount of cCPP-CeNPs was absorbed from cells on the coverslips A. Collectively, these findings suggest that CeNPs modified with cyclic cell-penetrating peptides exhibited the strongest transcytotic activity, which aligns with our earlier observations of this material group demonstrating superior tissue penetration ability and cellular uptake efficiency.

Considering the potential blocking effect of the corneal barrier, we conducted immunofluorescence staining of zonula occludens (ZO)−1, a protein associated with tight junction, to assess the tight junctional regions of the corneal epithelium. As displayed in Fig. 4B, the opening of the tight junctions in epithelial cell layers (indicated by the absence of a continuous ring-like structure between adjacent cells) was observed following lCPP-CeNPs and cCPP-CeNPs treatment. Subsequently, we examined the distribution of ZO-1 in human corneal epithelial cells (HCECs). HCECs were cultured in vitro to form a monolayer, mimicking the structure of the corneal epithelial barrier, and then treated with CeNPs or PBS for 2 h. The results showed considerable disruption in ZO-1 distribution, accompanied by a decrease in ZO-1 expression level, following lCPP-CeNPs and cCPP-CeNPs treatment, with more pronounced changes in the latter (Fig. 4C).

We conducted additional experiments to investigate the effect of UVB irradiation on the ZO-1 protein. As shown in Figure S9, UVB irradiation exerted a detrimental impact on the tight junctions between corneal epithelial cells, as demonstrated by a significant reduction in ZO-1 fluorescence continuity compared to the non-irradiated group. However, our cell-penetrating peptide-modified nano-cerium oxide continued to affect the ZO-1 protein, resulting in a further decrease in fluorescence continuity. Therefore, we conclude that our nano-cerium oxide can further enhance corneal permeability even in the presence of UVB radiation.

To further validate our hypothesis, we examined the changes in tight junctions using TEM imaging. Compared to the tight junctions in the PBS-treated group, mice treated with cCPP-CeNPs exhibited narrower gaps in the cornea, indicating that cCPP-CeNPs could rearrange the distribution of tight junctions in the corneal epithelium. In contrast, fewer cracks were observed in mice treated with lCPP-CeNPs and PEG-CeNPs (Fig. 4D). Therefore, these findings suggest that our nanoparticles penetrated the corneal barrier by compromising the tight junctions of the corneal epithelium, thereby promoting their antioxidant performance in the anterior capsules of the mouse lens.

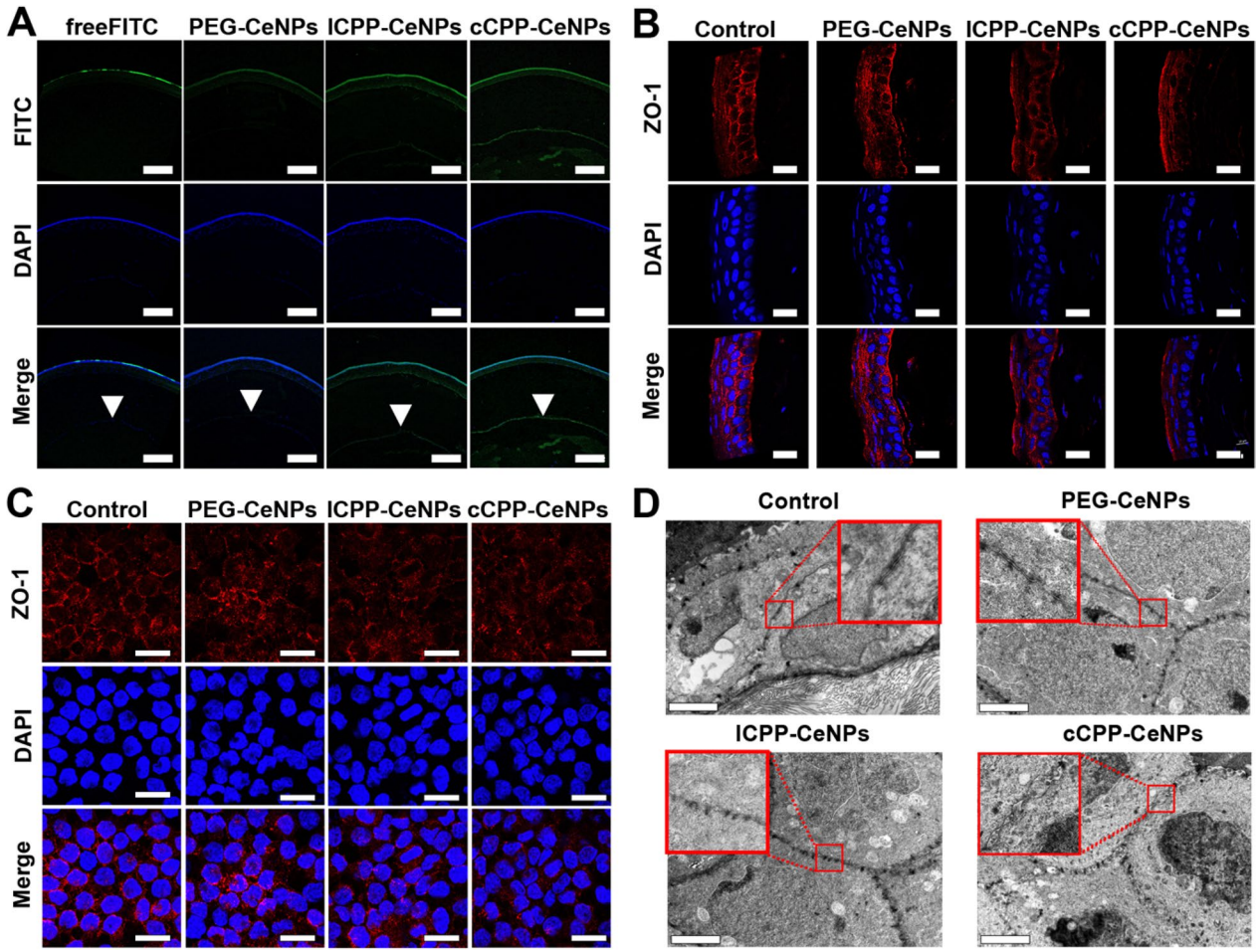

Fig. 4 Ophthalmic penetrating mechanism of CeNPs. **A** Confocal images of the cornea and anterior capsule after administering eyedrops containing free-FITC, PEG-CeNPs, lCPP-CeNPs, and cCPP-CeNPs (scale bar: 500 μm). White arrows point to the anterior capsule of the lens. **B** Immunofluorescence imaging of ZO-1 in the corneal epithelium of mice (scale bar: 40 μm). **C** Immunofluorescence imaging of ZO-1 in HCECs (scale bar: 50 μm). **D** TEM images of mice corneal tissue following treatment with PBS, PEG-CeNPs, lCPP-CeNPs, and cCPP-CeNPs. Red frames indicate corneal epithelial tight junctions (scale bars: 2 μm)

Cellular uptake and intracellular spatial localization of CeNPs

Our previous results have demonstrated that cCPP-CeNPs possess the ability to penetrate the corneal barrier and reach the anterior capsule of the lens. We further investigated whether lens epithelial cells (LECs) could uptake these particles. First, no cytotoxicity was observed in HCECs and human lens epithelial cell line (HLEB3) following administration with various concentrations of CeNPs (Fig. S10 and S11). Subsequently, we treated HLEB3 cells with FITC-modified PEG-CeNPs, lCPP-CeNPs, and cCPP-CeNPs for varying durations (1, 2, 3, and 4 h). The results indicated that the fluorescence intensity of cCPP-CeNPs peaked at 2 h (Fig. S12) and remained constant at 3 and 4 h. In contrast, treatments with PEG-CeNPs (Fig. S13) and lCPP-CeNPs (Fig. S14) exhibited the highest fluorescence intensity at 4 h, albeit weaker than that of the cCPP-CeNPs group. Consequently, we exposed HLEB3 cells to CeNPs for 2 h in subsequent experiments to investigate their cellular uptake efficiency (Fig. 5A). It has been reported that cyclicCPP exhibits the characteristic of early escape from lysosomes[62]. Therefore, to compare intracellular distribution of the nanoparticles, we examined their colocalization with mitochondria (Fig. 5C and D–F), endoplasmic reticulum, lysosomes, and the Golgi apparatus (Fig. S15–S17). Notably, we observed a significant fluorescence overlap between cCPP-CeNPs and mitochondria (Fig. 5C and F).

Additionally, mitochondrial membrane potential ($\Delta\Psi m$) serves as a crucial indicator of mitochondrial function. Therefore, we employed the membrane-permeant JC-1 staining to assess the $\Delta\Psi m$ of HLEB3 cells. Higher JC-1 red fluorescence intensity indicates a

reduced degree of mitochondrial dysfunction and a maintenance of ΔΨm. The JC-1 red fluorescence intensity in HLEB3 cells decreased significantly after ultraviolet B (UVB) exposure, while cCPP-CeNPs treatment improved the intensity close to that of the control group, notably higher than PEG-CeNPs and lCPP-CeNPs treatment (Fig. 5G and H). This result demonstrated that nanoparticles could shield cell mitochondria from the detrimental effects of ultraviolet radiation and uphold the stability of mitochondrial membrane potential. Previous studies have shown that mitochondria play a crucial role in regulating intracellular iron homeostasis [68]. Consequently, we measured the mitochondrial iron content using Mitoferro staining and observed a marked increase in mitochondrial iron following UVB stimulation (Fig. 5I and J). However, the increase was substantially reduced by cCPP-CeNPs treatment compared to the PEG-CeNPs and lCPP-CeNPs treated groups. Together, these results confirm that after cellular uptake, CeNPs can accumulate in mitochondria, enhancing their capacity to resist oxidative damage and ultimately maintain cellular physiological function.

Inhibition of ferroptosis of HLECs with CeNPs treatment

Previous studies have demonstrated that ferroptosis plays an essential role in Human Lymphatic Endothelial Cells (HLECs) in the formation of cataracts [21]. In this study, we further investigated whether the cytoprotective effect of CeNPs was through the inhibition of ferroptosis. We stimulated HLEB3 cells with UVB radiation at various intensities (0, 20, 40, 60, 80, and 100 mJ/cm^2), followed by culturing them for an additional 24 h. The results of CCK-8 assay showed an intensity-dependent decrease in cell viability with increasing UVB radiation (Fig. S18). Notably, cell viability decreased to approximate 70% when treated with 60 mJ/cm^2 UVB, which was used as the suitable UVB radiation dose in subsequent experiments. Next, HLEB3 cells were pretreated with specific inhibitors, including chloroquine (autophagy), Fer-1 (ferroptosis inhibitor), Z-VAD-FMK (a cell-permeant pan caspase inhibitor of apoptosis), and Nec-1 s (necrosis inhibitor) after UVB stimulation. The CCK-8 results demonstrated that Fer-1 exhibited the most significant effect, indicating that UVB radiation can effectively induce ferroptosis in HLEB3 cells (Fig. S19). To determine the cytoprotective effect of CeNPs, HLEB3 cells were pretreated with PEG-CeNPs, lCPP-CeNPs, and cCPP-CeNPs at equal concentrations (500 μM), and then stimulated with 60 mJ/cm^2 UVB. The cCPP-CeNPs group exhibited a significant restoration of cell viability, while minimal effect was observed in the PEG-CeNPs or lCPP-CeNPs groups (Fig. 6A–C). We then investigated the expression of ferroptosis markers, including the inducer achaete-scute complex-like 4 (ASCL4) and inhibitors glutathione peroxidase 4 (GPX4) and cystine-glutamate antiporter (xCT). Notably, the results showed a significant upregulation of ASCL4 and downregulation of GPX4, xCT after UVB induction. However, pretreatment with cCPP-CeNPs dramatically suppressed ASCL4 expression and promoted the expression of GPX4 and xCT, outperforming other groups, including those treated with PEG-CeNPs or lCPP-CeNPs (Fig. 6D and E). We further examined another important marker for ferroptosis, the ferrous ion content in HLEB3 cells, using Ferrorange staining and found that UVB exposure significantly increased ferrous iron accumulation, whereas cCPP-CeNPs pretreatment most effectively offset this effect compared to other treatments (Fig. 6F and G). It is noteworthy that previous studies have emphasized the significance of lipid peroxidation as a key event in the process of ferroptosis[69]. The increased ratio of non-oxidized to oxidized cells, as indicated by Lipid Peroxidation Probe-BDP$^{581/591}$ staining, suggested the occurrence of lipid peroxidation after UVB radiation (Fig. 6H and I). And pretreatment with cCPP-CeNPs effectively reversed this process. Collectively, these results demonstrated that cCPP-CeNPs inhibited HLEB3 ferroptosis by alleviating cell oxidative stress and lipid peroxidation.

CeNPs in the form of eye drops non-invasively alleviate UVB-induced cataracts in mice

Our previous in vitro experiments demonstrated that CeNPs were effective antioxidants in UVB-induced models. The cyclicCPP-modified nanoparticles could effectively penetrate the corneal barrier while simultaneously enhancing cellular uptake efficiency. These properties of cCPP-CeNPs can potentially mitigate cell damage caused by UV radiation by inhibiting ferroptosis. These

(See figure on next page.)

Fig. 5 Cellular uptake and intracellular spatial localization of CeNPs. Confocal images (**A**) and statistics (**B**) of HLEB3 cells 2 h after treatment with freeFITC, PEG-CeNPs, lCPP-CeNPs, and cCPP-CeNPs (scale bar: 100 μm). (**C**) Images of mitochondria staining of HLEB3 cells treated for 2 h with PEG-CeNPs, lCPP-CeNPs, and cCPP-CeNPs (scale bars: 40 μm), and the co-localization analysis (**D**–**F**) on the fluorescence intensity of ceria nanoparticles with mitochondria. (**G**) ΔΨm in indicated groups of HLEB3 cells and (**H**) statistics. Investigated using JC-1 staining (scale bar: 100 μm). Confocal images (**I**) and statistics (**J**) of mitochondrial iron content detected by MitoFerro staining (scale bar: 100 μm). In all histograms, data is presented as the mean ± SD ($n = 4$). *$p < 0.05$, **$p < 0.01$, ***$p < 0.001$, ****$p < 0.0001$; ns, no significance

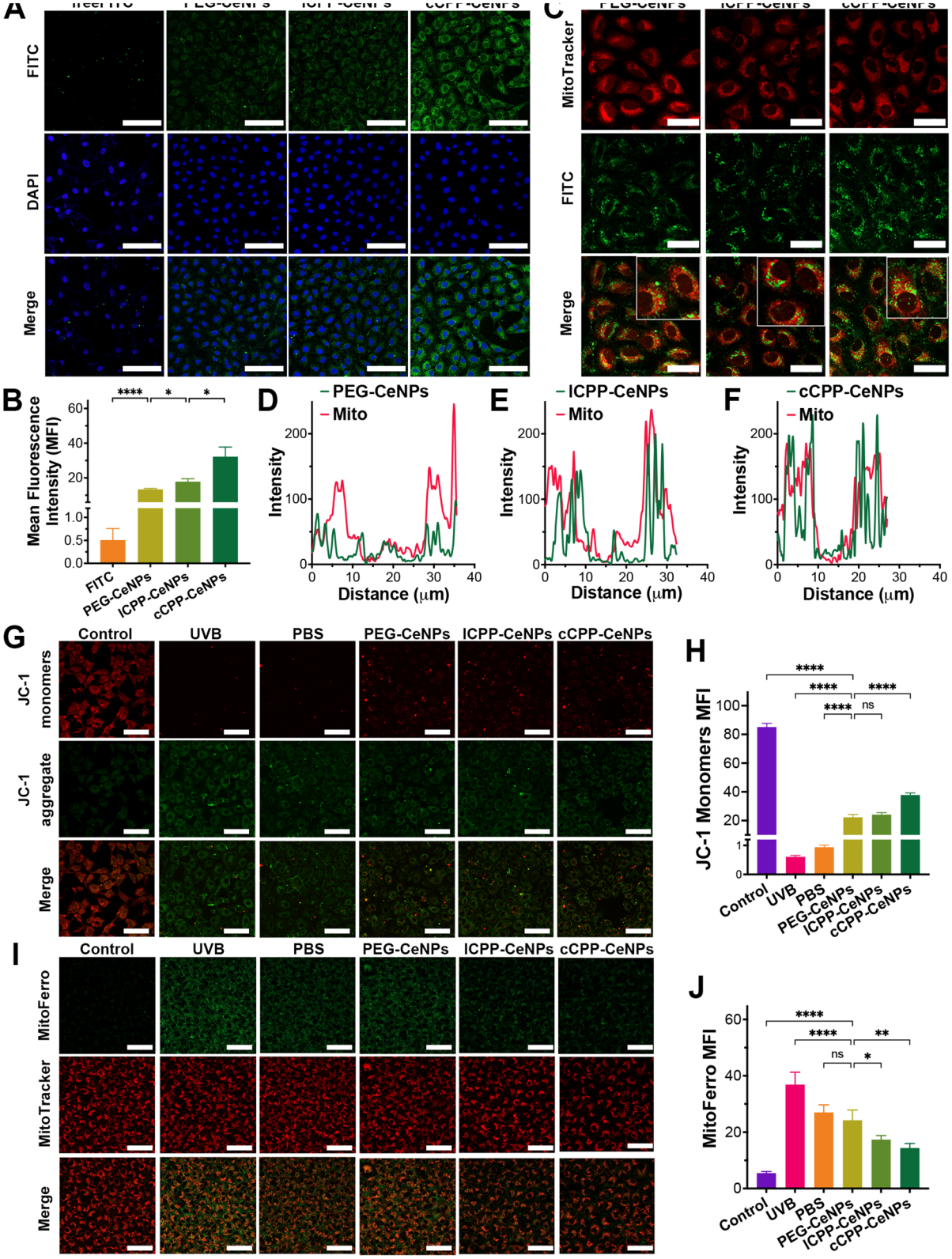

Fig. 5 (See legend on previous page.)

encouraging results prompted us to further investigate the in vivo therapeutic potential of these nanomaterials on cataracts. In this study, we employed a mouse cataract model induced by ultraviolet irradiation to explore whether nanomaterials could reduce cataract formation and elucidate the underlying mechanism.

Based on previous research [70], we have successfully established a mouse cataract model induced by UVB radiation at a wavelength of approximately 302 nm. On the third day after different doses of UV radiation (3.6 kJ/m^2 and 5.0 kJ/m^2), extensive anterior subcapsular opacification of the mouse lens was observed, which gradually underwent repair over the subsequent days, ultimately shrinking toward the center to form a scar (Fig. S20). In this study, 6-week-old female C57BL/6 mice were randomly divided into six groups ($n = 6$) for the experiments, and administered with PBS, PEG-CeNPs (3 mg/mL), lCPP-CeNPs (3 mg/mL), cCPP-CeNPs (3 mg/mL), and pirenoxine sodium eye drops, respectively. On the seventh day after exposure to UV radiations (3.6 kJ/m^2), the cCPP-CeNPs group showed a significant reduction in the subcapsular opacity area (Figs. 7B and S21). These results highlighted the remarkable efficacy of cCPP-CeNPs in resisting UVB-induced damage. In contrast, pirenoxine eye drops, a commercially available anticataract drug, demonstrated no significant therapeutic efficacy in the UV-induced mouse cataract model (Fig. 7B and S21). We utilized inductively coupled plasma mass spectrometry (ICP-MS) to measure the cerium concentration in the aqueous humor of the mice in each groups. As illustrated in Fig. S22, the cCPP-CeNPs treatment group exhibited the highest cerium content in the aqueous humor, which may stem from the effect of the cell-penetrating peptide on corneal permeability. Subsequently, Hematoxylin and Eosin (H&E) staining revealed that UVB stimulation significantly decreased the number of LECs in the capsule, whereas cCPP-CeNPs treatment significantly inhibited this detrimental effect (Fig. S23). The promising outcomes observed in animal models motivated us to investigate the antioxidation mechanism of nanomaterials in mouse lenses. We examined ferroptosis in LECs of UVB-stimulated mice eyes. Initially, we used immunofluorescence staining to assess the expression changes of ferroptosis markers. The results showed that topical delivery with PEG-CeNPs, lCPP-CeNPs, and cCPP-CeNPs significantly inhibited UVB-induced LECs ferroptosis, with cCPP-CeNPs showing the most pronounced protective effect (Fig. 7C and D). Furthermore, we conducted the immunofluorescence assays of mouse eyes on two other critical ferroptosis markers, 4-HNE and FTH (Fig. S24). Consistent with the expression patterns of the other three ferroptosis indicators, we observed that the ferroptosis inhibition effect of the cCPP-CeNPs group remained the most pronounced. Finally, Lillie's staining was used to visualize ferrous ions in the anterior lens capsule. The cCPP-CeNPs treatment group exhibited a substantial reduction in the ferrous ion content in mouse LECs (Fig. S25). These findings aligned with our cell experiments, further supporting that cCPP-CeNPs mitigated the detrimental effects of ultraviolet radiation on LECs by inhibiting ferroptosis. In summary, these results corroborate that cCPP-CeNPs penetrate the corneal barrier effectively, scavenge cellular ROS, alleviate lipid peroxidation, maintain mitochondrial function, and inhibit LEC ferroptosis both in *vitro* and in *vivo*.

CeNPs do not promote toxicity to ocular and systemic tissues

Finally, we addressed concerns regarding the potential toxicity of CeNPs to other ocular tissues and major organs. After administering various eye drops (PBS, PEG-CeNPs, lCPP-CeNPs, and cCPP-CeNPs) for more than ten consecutive days, no noticeable signs of inflammation or physiological abnormalities were observed in the cornea, retina, or other major organs through histological examinations (Fig. S26–S29). These findings indicate the biocompatibility and safety of the administered CeNPs.

Discussion

In the present study, we have successfully developed a rationally designed advanced nano formulation, which exhibits exceptional water solubility and potent antioxidant activity mimicking multienzymes. Thanks to their

(See figure on next page.)

Fig. 6 Anti-ferroptosis effect of CeNPs in UVB-stimulated HLEB3 cells. **A** Representative images and statistics (**B**) of living/dead cell assay of HLEB3 cells treated with UVB and different CeNPs. Living and dead HLEB3 cells were stained with calcein acetoxymethyl ester (calcein-AM, green) and propidium iodide (PI, red), respectively (scale bars: 100 μm). **C** Cell viability of HLEB3 cells was evaluated using the CCK-8 assay following 60 mJ/cm^2 UVB exposure and pre-treatment with PEG-CeNPs, lCPP-CeNPs, and cCPP-CeNPs (equal ceria concentration, 500 μM). In the histogram, data is presented as the mean ± SD ($n = 4$). Western blot (**D**) and statistics (**E**) of the expression of ferroptosis-related proteins; Glyceraldehyde 3-phosphate dehydrogenase (GAPDH) served as the internal control. **F** Ferrorange staining and statistics (**G**) was utilized to determine the total iron level in HLEB3 cells treated with UVB and CeNPs (scale bars: 100 μm). **H** Representative fluorescence microscopy images and statistics (**I**) of $BDP^{581/591}$ staining, indicating lipid peroxidation in HLEB3 cells (non-oxidized and oxidized cells stained red and green, respectively (scale bars: 200 μm)). In all other histograms, data is presented as the mean ± SD ($n = 3$). *$p < 0.05$, **$p < 0.01$, ***$p < 0.001$, ****$p < 0.0001$; ns, no significance

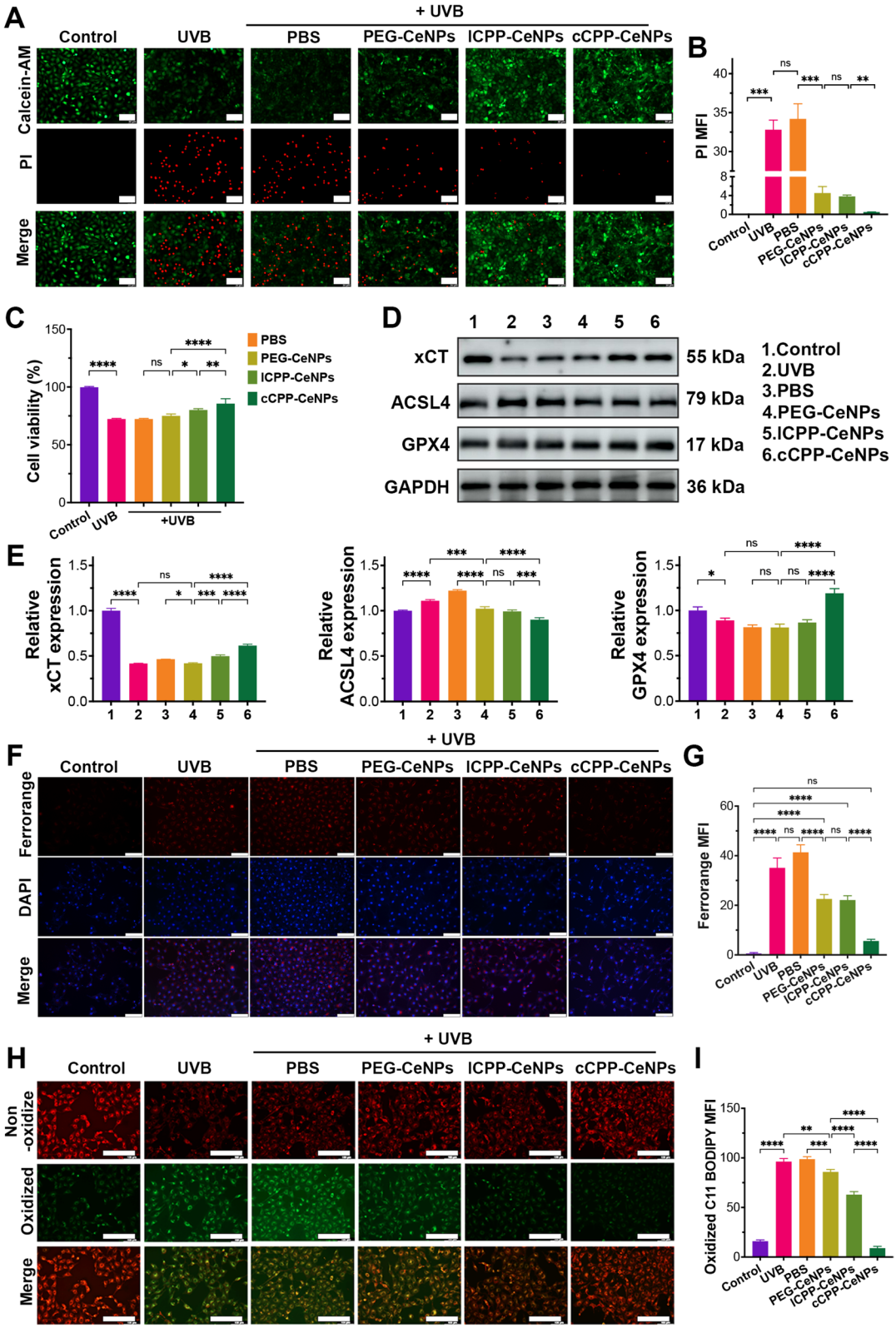

Fig. 6 (See legend on previous page.)

nanoscale size and cyclic cell-penetrating peptides, the nanoparticles demonstrate an excellent ability to penetrate the corneal barrier, thereby enabling them to effectively exert antioxidant activity within the lens capsules. Our findings indicate that efficient intracellular delivery of cCPP-CeNPs effectively inhibits UVB-induced ferroptosis in LECs, reducing intracellular lipid peroxidation and suppressing ACSL4 and TfR1 expression. Importantly, these effects were also observed in the UVB mouse cataract model, resulting in a notable decrease in cataract incidence. As a result, this system overcomes the challenges of noninvasive drug delivery to the anterior chamber of the eye, highlighting the pivotal role of ferroptosis in UV-induced cell and animal injury models and offering a novel perspective for further research into cataract prevention and treatment strategies. In addition, the mitochondrial protective effects exhibited by nanoparticles provide potential treatments for other eye diseases associated with mitochondrial dysfunction.

First of all, it is well-established that GPX4 is a selenoprotein with glutathione-dependent peroxidase activity, primarily responsible for preventing lipid oxidation in cellular membranes [71, 72]. Our experiments demonstrated a significant reduction in intracellular lipid peroxide levels in cells treated with CeNPs, particularly in the cCPP-CeNPs group. Concurrently, western blot analysis revealed an increase in GPX4 expression in cells of the cCPP-CeNPs group, surpassing even the control group. These results indicate that nanoparticles, functioning as exogenous antioxidants, not only decrease intracellular ROS levels but also reduce the consumption of endogenous antioxidants, thereby inhibiting the accumulation of intracellular lipid peroxidation, mitigating the detrimental effects of UVB irradiation on cells.

Meanwhile, GPX4 is an important target for inhibiting ferroptosis, considering that the inhibition or instability of GPX4 can sensitize or even trigger ferroptosis [73]. GPX4 plays a crucial role in regulating ferroptosis through its unique ability to reduce complex hydroperoxides, including phospholipid hydroperoxides and cholesterol hydroperoxides, effectively disrupting the lipid peroxidation chain reaction [58, 59]. Using immunofluorescence techniques and other methods, our investigation into the expression trends of ferroptosis-related markers such as ASCL4 and GPX4 suggests that the effective intracellular delivery of nanomaterials may play a pivotal role in maintaining the stability of System xc-/Glutathione (GSH)/GPX4 axis, which in turn helps counteract the damage induced by UV radiation and preserves cell viability.

Mitochondria play a primary role in regulating cell death (RCD), including ferroptosis. Mitochondria release or recruit specific cell death-promoting factors, which are associated with alterations in the mitochondrial outer membrane potential, changes in permeability, and the opening of the mitochondrial permeability transition pore (MPTP) [74]. In addition to their role in cell death regulation, mitochondria are essential for cellular energy metabolism and serve as the primary organelles for intracellular iron regulation. The transport of cytoplasmic free iron, specifically ferrous ions, into mitochondria, is primarily mediated by mitochondrial ferritin 1/2, endosomes, or other mediators involved in the synthesis of heme and iron-sulfur (Fe–S) clusters [75]. Several studies have reported an increase in mitochondrial Fe^{2+} levels during ferroptosis induced by compounds like doxorubicin, elastin, and Sulfasalazine (SAS) [76, 77]. Iron overload is a prominent characteristic of ferroptosis, as excessive ferrous ions lead to lipid peroxidation through the Fenton reaction within mitochondria, thereby triggering ferroptosis [78, 79]. In this study, a significant reduction in lipid peroxidation levels and ferrous ion content was observed in LECs treated with cCPP-CeNPs. In addition, these cells exhibited minimal mitochondrial membrane potential depolarization and the lowest accumulation of ferrous ions within the mitochondria. Additionally, we employed histochemistry to stain mouse lenses for ferrous ions, revealing that the efficient intracellular delivery of nanomaterials reduced the accumulation of intracellular ferrous ions. Thanks to the enrichment of nanoparticles around mitochondria, oxidative stress within mitochondria is effectively reduced, and the stability of the respiratory chain is maintained. Meanwhile, the protective impact of our nanoparticles on cell mitochondria might play a key role in sustaining the absorption and transport of excess ferrous ions by cells. By preserving mitochondrial function, our nanoparticles maintain intracellular iron homeostasis, thereby

(See figure on next page.)

Fig. 7 Anticataract effects of CeNPs in the anterior capsule of UVB-stimulated mice via alleviating HLECs ferroptosis. **A** Representative slit lamp microscope images of mouse eyes at 7 th day after UV radiation modeling ($n = 6$). Control (untreated); PBS group; PEG-CeNPs group (3 mg/mL); lCPP-CeNPs group (3 mg/mL); cCPP-CeNPs group (3 mg/mL); pirenoxine sodium eye drops. **B** The formation of anterior subcapsular cataract in the lenses after 3.6 kJ/m^2 illumination of UV exposure and indicated treatments. Immunofluorescence staining (**C**) and statistics (**D**) of ferroptosis-related proteins ACSL4, GPX4 and xCT (scale bar, 20 μm). In all histograms, data is presented as the mean ± SD ($n = 3$). *$p < 0.05$, **$p < 0.01$, ***$p < 0.001$, ****$p < 0.0001$; ns, no significance

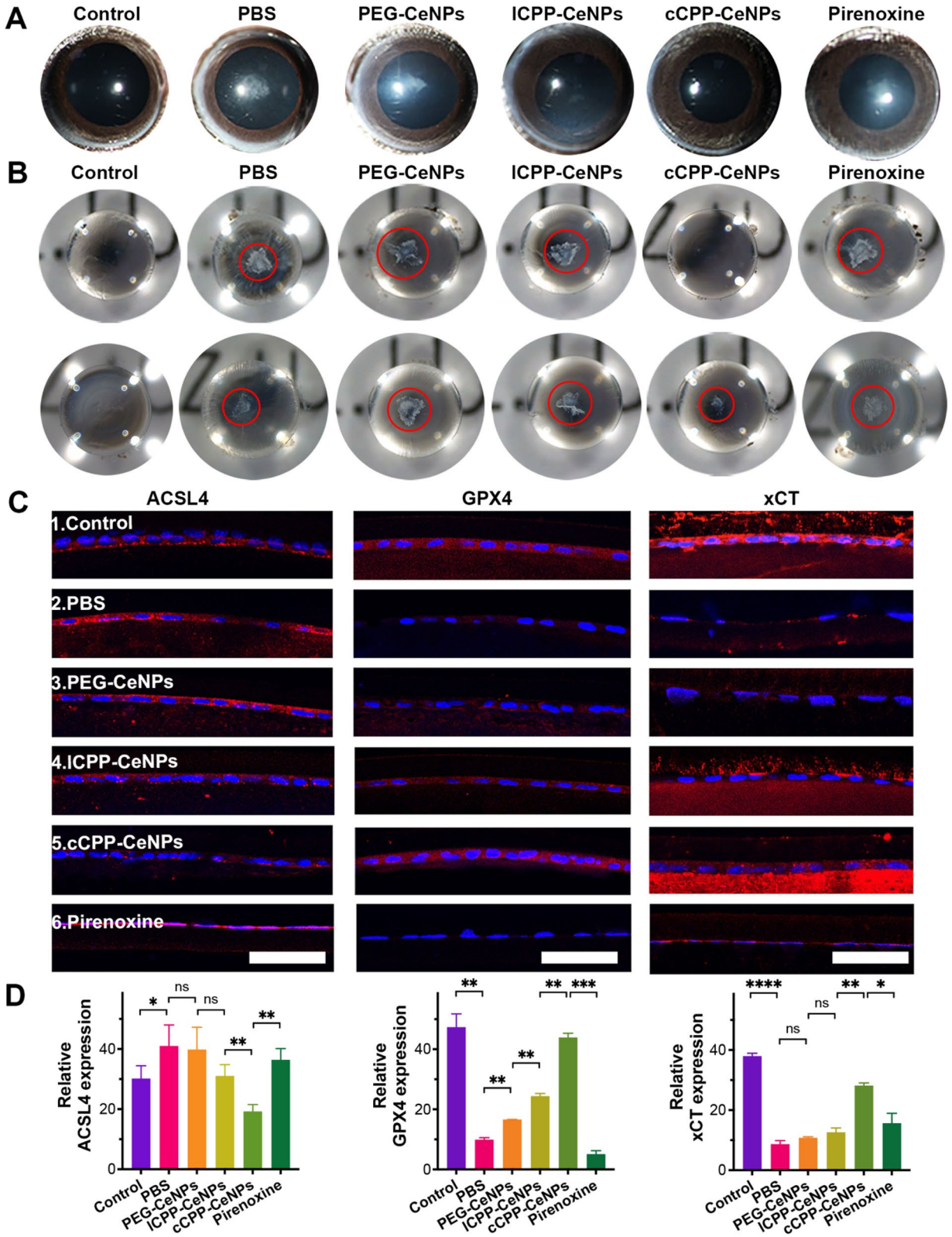

Fig. 7 (See legend on previous page.)

mitigating the accumulation of potentially harmful ferrous ions and preventing the initiation of ferroptosis.

Finally, corneal epithelial cells communicate through specialized intercellular junctions known as zonules or tight junctions. These junctions, located just beneath the apical surface, are recognized to form a protective barrier for the passive movement of fluids, electrolytes, macromolecules, and cells through paracellular pathways [80]. Tight junctions consist of various membrane proteins, including claudins and occludin, as well as membrane-associated proteins, such as ZO-1 [81], ZO-2, and ZO-3 [82]. In the cornea, ZO-1 is predominantly located in the superficial layer of the epithelium [83–85], mainly contributing to the resistance barrier of the corneal epithelium. The zone of occlusion (ZO) acts as a bridge between tight junction (TJ) proteins, which are responsible for barrier formation, and the actin-myosin cytoskeleton [86–88]. Consequently, ZO-1 is commonly used as a marker for TJ in studies investigating the morphological changes of increased transepithelial paracellular penetration [89–92]. In our preliminary experiments, we explored the impact of nanoparticles on corneal epithelial permeability. Given the hydrophilic characteristic of the material, we hypothesized that nanoparticles would predominantly traverse the corneal barrier via the paracellular pathway [90, 93]. Consequently, we assessed the integrity of tight junctions within the corneal epithelium, aiming to identify the factors contributing to variations in the penetration capabilities of different nanoparticle groups. As mentioned above, our in vivo and in vitro experiments verified the disruptive effect of cell-penetrating peptide-modified nanomaterials on ZO-1, with cyclized cell-penetrating peptide-modified nanoparticles showing a more pronounced effect. These findings strongly suggest that nanoparticles modified with cell-penetrating peptides possess a destructive effect on ZO-1, potentially enhancing corneal permeability through the paracellular pathway. This enhancement could contribute to the efficiency of intraocular drug delivery. Moreover, the detrimental impact of nanoparticles on the corneal barrier remains incompletely understood. Moving forward, we will delve deeper into elucidating the specific effects of cell-penetrating peptides on corneal permeability.

Conclusions

In summary, we have developed a water-soluble nanoparticle, cCPP-CeNPs, which has a modified surface with cell-penetrating peptides. This modification not only preserves the distinctive multi-enzyme simulation activity and automatic regeneration ability of ceria nanoparticles but also enhances the cellular uptake efficiency of nanoparticles. Furthermore, it improves their tissue penetration ability by influencing intercellular tight junctions, thus enhancing their capability to traverse the corneal barrier. Our in vivo mouse model studies of UVB-induced cataract revealed that nanomaterials, applied as local eye drops, can protect mice lens from oxidative damage caused by ultraviolet light within a specific dose range, consequently preventing the development of early cataracts. With further refinement, this drug delivery strategy may represent another avenue for the preventive and conservative treatment of lens diseases. Moreover, the potential applications of this approach could extend to other oxidative stress-related chronic pathological conditions, such as diabetes-related fundus disease or glaucoma.

Abbreviations

2-(4-iodophenyl)-3-(4-nitrophenyl)-5-(2,4-disulfophenyl)-2H-tetrazolium Monosodium salt	
BCA	Bicinchoninic acid assay
CCK-8	Cell Counting Kit-8
cCPPs	Cyclic cell-penetrating peptides
Ce^{3+}	Trivalent
Ce^{4+}	Tetravalent
CeNPs	Ceria nanoparticles
CPPs	Cell-penetrating peptides
ddH_2O	Double distilled water
DMEM	Dulbecco's modified eagle's medium
DMPO	5,5-Dimethyl-1-Pyrroline-N-Oxide
$DSPE\text{-}PEG_{2000}$	1,2-Distearoyl-sn-glycero-3-phosphoethanolamine-N-[methoxy(polyethylene-glycol)-2000
ESR	Electron spin resonance
FBS	Fetal bovine serum
Fe–S	Iron-sulfur
FITC	Fluorescein isothiocyanate
GPX4	Glutathione peroxidase 4
H&E	Hematoxylin and Eosin
HCECs	Human corneal epithelial cells
HLEB3	Human lens epithelial cell line
HORAC	Hydroxyl radical antioxidant capacity
HR-TEM	High-resolution transmission electron microscope
ICP-MS	Inductively coupled plasma mass spectrometry
LECs	Lens epithelial cells
MALDI-TOF MS	Matrix-assisted laser desorption/ionization-time of flight mass spectrometry
MPTP	Mitochondrial permeability transition pore
OH	Hydroxyl radicals
PBS	Phosphate-buffered saline
PMSF	Protease inhibitors
PVDF	Polyvinylidene fluoride or polyvinylidene difluoride
RCD	Regulating cell death
RIPA	Radio-immunoprecipitation assay
ROS	Reactive oxygen species
SAED	Selected area electron diffraction
SD	Standard deviation
SDS-PAGE	Sodium dodecyl sulfate–polyacrylamide gel electrophoresis
TEM	Transmission electron microscopy
TJ	Tight junction
UVB	Ultraviolet B

WST-1	Water-soluble tetrazolium salt
XPS	X-ray photoelectron spectroscopy
XRD	X-ray diffraction
ZO	Zonula occludens

Supplementary Information

The online version contains supplementary material available at https://doi.org/10.1186/s12951-025-03402-1.

Additional file 1.

Author contributions

LJ and JL designed and performed experiments, analyzed data, wrote the manuscript and prepared all figures. WC reviewed and edited the manuscript. SC, JG and XC analyzed data. YZ, WY, and ZP were responsible for the investigation and data curation. MZ reviewed and edited the manuscript. KY supervised the project. HH was responsible for the design of the experiment, reviewed and edited the manuscript and supervised the project. YW and YY was responsible for the design of the experiment, reviewed and edited the manuscript, supervised the project and acquired funding. All authors read and approved the final manuscript.

Funding

This work was supported by the National Natural Science Foundation of China (Grant numbers 82070938, 82371036 and 82401317) and the Program of the Natural Science Foundation of Zhejiang Province (Grant number LTGY23H120003).

Availability of data and materials

No datasets were generated or analysed during the current study.

Declarations

Ethics approval and consent to participate

All animal experiments have complied with the Association for Research in Vision and Ophthalmology Statement and the guidelines for the Animal Care and Use Committee, Zhejiang University. All animal experimental protocols were approved by the Animal Ethics Committee, the Second Affiliated Hospital, School of Medicine, Zhejiang University (Approval number: 2023–084).

Consent for publication

Not applicable.

Competing interests

The authors declare no competing interests.

Author details

[1]Eye Center of the Second Affiliated Hospital, Zhejiang University School of Medicine, Hangzhou, Zhejiang, China. [2]Shangyu People's Hospital of Shaoxing, Shaoxing University, Shimin Street 517, Shangyu District, Shaoxing 312300, Zhejiang, China. [3]The Bear Creek School, 8905 208 Th Ave NE, Redmond, WA 98053, USA.

Received: 2 September 2024 Accepted: 15 April 2025
Published online: 07 May 2025

References

1. Pesudovs K, et al. Cataract-related blindness and vision impairment in 2020 and trends over time in relation to VISION 2020: the right to sight: an analysis for the global burden of disease study. Invest Ophthalmol Vis Sci. 2021;62(8):3523.
2. Pesudovs K, et al. Global estimates on the number of people blind or visually impaired by cataract: a meta-analysis from 2000 to 2020. Eye. 2024;57:14.
3. Ruiss M, Findl O, Kronschläger M. The human lens: an antioxidant-dependent tissue revealed by the role of caffeine. Ageing Res Rev. 2022;79: 101664.
4. Michael R, Bron AJ. The ageing lens and cataract: a model of normal and pathological ageing. Phil Trans R Soc B Biol Sci. 2011;366(1568):1278–92.
5. Cicinelli MV, et al. Cataracts. Lancet. 2023;401(10374):377–89.
6. Gorrini C, Harris IS, Mak TW. Modulation of oxidative stress as an anticancer strategy. Nat Rev Drug Discov. 2013;12(12):931–47.
7. Vitale G, Salvioli S, Franceschi C. Oxidative stress and the ageing endocrine system. Nat Rev Endocrinol. 2013;9(4):228–40.
8. Wang H, et al. Nanorepair medicine for treatment of organ injury. Natl Sci Rev. 2024. https://doi.org/10.1093/nsr/nwae280.
9. Cao J, et al. Turning gray selenium and sublimed sulfur into a nanocomposite to accelerate tissue regeneration by isothermal recrystallization. J Nanobiotechnol. 2023;21(1):57.
10. Savion N, et al. S-allylmercapro-N-acetylcysteine attenuates the oxidation-induced lens opacification and retinal pigment epithelial cell death in vitro. Antioxidants. 2019;8(1):25.
11. Zhao L, et al. Lanosterol reverses protein aggregation in cataracts. Nature. 2015;523(7562):607–11.
12. Carey JW, et al. In vivo inhibition of l-buthionine-(S, R)-sulfoximine-induced cataracts by a novel antioxidant, N-acetylcysteine amide. Free Radical Biol Med. 2011;50(6):722–9.
13. Zhang X, et al. Anti-cataract effects of coconut water in vivo and in vitro. Biomed Pharmacother. 2021;143: 112032.
14. Luo L-J, Nguyen DD, Lai J-Y. Dually functional hollow ceria nanoparticle platform for intraocular drug delivery: a push beyond the limits of static and dynamic ocular barriers toward glaucoma therapy. Biomaterials. 2020;243: 119961.
15. Lai J-Y, Luo L-J, Nguyen DD. Multifunctional glutathione-dependent hydrogel eye drops with enhanced drug bioavailability for glaucoma therapy. Chem Eng J. 2020;402: 126190.
16. Jumelle C, et al. Advances and limitations of drug delivery systems formulated as eye drops. J Control Release. 2020;321:1–22.
17. Gause S, et al. Mechanistic modeling of ophthalmic drug delivery to the anterior chamber by eye drops and contact lenses. Adv Coll Interface Sci. 2016;233:139–54.
18. Friedmann Angeli JP, et al. Inactivation of the ferroptosis regulator Gpx4 triggers acute renal failure in mice. Nat Cell Biol. 2014;16(12):1180–91.
19. Reichert CO, et al. Ferroptosis mechanisms involved in neurodegenerative diseases. Int J Mol Sci. 2020;21(22):8765.
20. Jiang X, Stockwell BR, Conrad M. Ferroptosis: mechanisms, biology and role in disease. Nat Rev Mol Cell Biol. 2021;22(4):266–82.
21. Wei Z, et al. Aging lens epithelium is susceptible to ferroptosis. Free Radical Biol Med. 2021;167:94–108.
22. Stockwell BR, Jiang X, Gu W. Emerging mechanisms and disease relevance of ferroptosis. Trends Cell Biol. 2020;30(6):478–90.
23. Yang WS, et al. Regulation of ferroptotic cancer cell death by GPX4. Cell. 2014;156(1):317–31.
24. Ursini F, Maiorino M. Lipid peroxidation and ferroptosis: the role of GSH and GPx4. Free Radical Biol Med. 2020;152:175–85.
25. Riegman M, et al. Ferroptosis occurs through an osmotic mechanism and propagates independently of cell rupture. Nat Cell Biol. 2020;22(9):1042–8.
26. Wei Z, et al. Deficiency in glutathione peroxidase 4 (GPX4) results in abnormal lens development and newborn cataract. Proc Natl Acad Sci. 2024;121(48): e2407842121.
27. Wei Z, et al. Prevention of age-related truncation of γ-glutamylcysteine ligase catalytic subunit (GCLC) delays cataract formation. Sci Adv. 2024;10(17): eadl1088.
28. Thomas C, editor. Sensor fusion and its applications. Rijeka: IntechOpen; 2010.
29. Yañez-Soto B, et al. Interfacial phenomena and the ocular surface. Ocul Surf. 2014;12(3):178–201.
30. Cunha-Vaz J, Bernardes R, Lobo C. Blood-retinal barrier. Eur J Ophthalmol. 2011;21(6):3–9.
31. Han H, et al. Polymer- and lipid-based nanocarriers for ocular drug delivery: current status and future perspectives. Adv Drug Deliv Rev. 2023;196: 114770.

32. Popov A. Mucus-penetrating particles and the role of ocular mucus as a barrier to micro- and nanosuspensions. J Ocul Pharmacol Ther. 2020;36(6):366–75.
33. Wang C, Pang Y. Nano-based eye drop: topical and noninvasive therapy for ocular diseases. Adv Drug Deliv Rev. 2023;194: 114721.
34. Jia F, et al. Macromolecular platform with super-cation enhanced transcornea infiltration for noninvasive nitric oxide delivery in ocular therapy. ACS Nano. 2020;14(12):16929–38.
35. Mofidfar M, et al. Drug delivery to the anterior segment of the eye: a review of current and future treatment strategies. Int J Pharm. 2021;607: 120924.
36. Gallucci N, et al. Towards the development of antioxidant cerium oxide nanoparticles for biomedical applications: controlling the properties by tuning synthesis conditions. Nanomaterials. 2021;11(2):542.
37. Lv Z, et al. Recent progress of nanomedicine in managing dry eye disease. Adv Ophthalmol Pract Res. 2024;4(1):23–31.
38. Lee SS, et al. Antioxidant properties of cerium oxide nanocrystals as a function of nanocrystal diameter and surface coating. ACS Nano. 2013;7(11):9693–703.
39. Esch F, et al. Electron localization determines defect formation on ceria substrates. Science. 2005;309(5735):752–5.
40. Karakoti A, et al. Redox-active radical scavenging nanomaterials. Chem Soc Rev. 2010;39(11):4422–32.
41. Celardo I, et al. Pharmacological potential of cerium oxide nanoparticles. Nanoscale. 2011;3(4):1411–20.
42. Karakoti AS, et al. PEGylated nanoceria as radical scavenger with tunable redox chemistry. J Am Chem Soc. 2009;131(40):14144–5.
43. Cui W, et al. Nanoceria-mediated cyclosporin a delivery for dry eye disease management through modulating immune–epithelial crosstalk. ACS Nano. 2024;18(17):11084–102.
44. Kwon HJ, et al. Mitochondria-targeting ceria nanoparticles as antioxidants for Alzheimer's disease. ACS Nano. 2016;10(2):2860–70.
45. Rzigalinski BA, Carfagna CS, Ehrich M. Cerium oxide nanoparticles in neuroprotection and considerations for efficacy and safety. Wiley Interdiscip Rev Nanomed Nanobiotechnol. 2017;9(4): e1444.
46. Li Y, et al. Acquired superoxide-scavenging ability of ceria nanoparticles. Angew Chem. 2015;127(6):1852–5.
47. Heckert EG, et al. The role of cerium redox state in the SOD mimetic activity of nanoceria. Biomaterials. 2008;29(18):2705–9.
48. Pirmohamed T, et al. Nanoceria exhibit redox state-dependent catalase mimetic activity. Chem Commun. 2010;46(16):2736–8.
49. Niu J, et al. Cardioprotective effects of cerium oxide nanoparticles in a transgenic murine model of cardiomyopathy. Cardiovasc Res. 2007;73(3):549–59.
50. Chigurupati S, et al. Effects of cerium oxide nanoparticles on the growth of keratinocytes, fibroblasts and vascular endothelial cells in cutaneous wound healing. Biomaterials. 2013;34(9):2194–201.
51. Yuan A, et al. Ceria nanozyme-integrated microneedles reshape the perifollicular microenvironment for androgenetic alopecia treatment. ACS Nano. 2021;15(8):13759–69.
52. Mitra RN, et al. Glycol chitosan engineered autoregenerative antioxidant significantly attenuates pathological damages in models of age-related macular degeneration. ACS Nano. 2017;11(5):4669–85.
53. Chen J, et al. Rare earth nanoparticles prevent retinal degeneration induced by intracellular peroxides. In: Nano-Enabled Medical Applications. New York: Jenny Stanford Publishing; 2020. p. 525–46.
54. Yang C-J, et al. Unveiling the power of gabapentin-loaded nanoceria with multiple therapeutic capabilities for the treatment of dry eye disease. ACS Nano. 2023;17(24):25118–35.
55. Ger T-Y, et al. Biofunctionalization of nanoceria with sperminated hyaluronan enhances drug delivery performance for corneal alkali burn therapy. Chem Eng J. 2023;476: 146864.
56. Nguyen DD, et al. Amination-mediated nano eye-drops with enhanced corneal permeability and effective burst release for acute glaucoma treatment. Chem Eng J. 2023;451: 138620.
57. Mandal A, et al. Polymeric micelles for ocular drug delivery: from structural frameworks to recent preclinical studies. J Control Release. 2017;248:96–116.
58. Mitchell MJ, et al. Engineering precision nanoparticles for drug delivery. Nat Rev Drug Discov. 2021;20(2):101–24.
59. Salama AH, Shamma RN. Tri/tetra-block co-polymeric nanocarriers as a potential ocular delivery system of lornoxicam: in-vitro characterization, and in-vivo estimation of corneal permeation. Int J Pharm. 2015;492(1–2):28–39.
60. Yang CJ, Nguyen DD, Lai JY. Poly (l-Histidine)-mediated on-demand therapeutic delivery of roughened ceria nanocages for treatment of chemical eye injury. Adv Sci. 2023;10(26):2302174.
61. Nguyen DD, et al. Highly retina-permeating and long-acting resveratrol/metformin nanotherapeutics for enhanced treatment of macular degeneration. ACS Nano. 2023;17(1):168–83.
62. Qian Z, et al. Discovery and mechanism of highly efficient cyclic cell-penetrating peptides. Biochemistry. 2016;55(18):2601–12.
63. Wang M, et al. Ceria nanoparticles ameliorate renal fibrosis by modulating the balance between oxidative phosphorylation and aerobic glycolysis. J Nanobiotechnol. 2022;20:1–18.
64. Zeng F, et al. Custom-made ceria nanoparticles show a neuroprotective effect by modulating phenotypic polarization of the microglia. Angew Chem. 2018;130(20):5910–4.
65. Li F, et al. Dual detoxification and inflammatory regulation by ceria nanozymes for drug-induced liver injury therapy. Nano Today. 2020;35: 100925.
66. Yu T, et al. Various-shaped uniform Mn_3O_4 nanocrystals synthesized at low temperature in air atmosphere. Chem Mater. 2009;21(11):2272–9.
67. Xu C, Qu X. Cerium oxide nanoparticle: a remarkably versatile rare earth nanomaterial for biological applications. NPG Asia Mater. 2014;6(3): e90.
68. Li F-J, et al. System Xc−/GSH/GPX4 axis: An important antioxidant system for the ferroptosis in drug-resistant solid tumor therapy. Front Pharmacol. 2022;13: 910292.
69. Dixon SJ, et al. Ferroptosis: an iron-dependent form of nonapoptotic cell death. Cell. 2012;149(5):1060–72.
70. Zhang J, et al. Ultraviolet radiation–induced cataract in mice: the effect of age and the potential biochemical mechanism. Invest Ophthalmol Vis Sci. 2012;53(11):7276–85.
71. Seibt TM, Proneth B, Conrad M. Role of GPX4 in ferroptosis and its pharmacological implication. Free Radical Biol Med. 2019;133:144–52.
72. Borchman D, Yappert MC. Lipids and the ocular lens. J Lipid Res. 2010;51(9):2473–88.
73. Mao C, et al. DHODH-mediated ferroptosis defence is a targetable vulnerability in cancer. Nature. 2021;593(7860):586–90.
74. Lemasters JJ, et al. The mitochondrial permeability transition in cell death: a common mechanism in necrosis, apoptosis and autophagy. Biochimica et Biophysica Acta (BBA) Bioenerg. 1998;1366(1–2):177–96.
75. Rouault TA, Tong W-H. Iron–sulphur cluster biogenesis and mitochondrial iron homeostasis. Nat Rev Mol Cell Biol. 2005;6(4):345–51.
76. Yuan H, et al. CISD1 inhibits ferroptosis by protection against mitochondrial lipid peroxidation. Biochem Biophys Res Commun. 2016;478(2):838–44.
77. Kim EH, et al. CISD2 inhibition overcomes resistance to sulfasalazine-induced ferroptotic cell death in head and neck cancer. Cancer Lett. 2018;432:180–90.
78. Wang H, et al. Mitochondria regulation in ferroptosis. Eur J Cell Biol. 2020;99(1): 151058.
79. Gao M, et al. Role of mitochondria in ferroptosis. Mol Cell. 2019;73(2):354-363.e3.
80. Ko J-A, Yanai R, Nishida T. Up-regulation of ZO-1 expression and barrier function in cultured human corneal epithelial cells by substance P. FEBS Lett. 2009;583(12):2148–53.
81. Stevenson BR, et al. Identification of ZO-1: a high molecular weight polypeptide associated with the tight junction (zonula occludens) in a variety of epithelia. J Cell Biol. 1986;103(3):755–66.
82. Wittchen ES, Haskins J, Stevenson BR. Protein interactions at the tight junction: actin has multiple binding partners, and ZO-1 forms independent complexes with ZO-2 and ZO-3. J Biol Chem. 1999;274(49):35179–85.
83. Wang Y, Chen M, Wolosin JM. ZO-1 in corneal epithelium; stratal distribution and synthesis induction by outer cell removal. Exp Eye Res. 1993;57(3):283–92.

84. Sugrue SP, Zieske JD. ZO1 in corneal epithelium: association to the zonula occludens and adherens junctions. Exp Eye Res. 1997;64(1):11–20.
85. Ban Y, et al. Tight junction-related protein expression and distribution in human corneal epithelium. Exp Eye Res. 2003;76(6):663–9.
86. González-Mariscal L, Tapia R, Chamorro D. Crosstalk of tight junction components with signaling pathways. Biochimica et Biophysica Acta BBA Biomembr. 2008;1778(3):729–56.
87. Itoh M, et al. Involvement of ZO-1 in cadherin-based cell adhesion through its direct binding to α catenin and actin filaments. J Cell Biol. 1997;138(1):181–92.
88. Fanning AS, et al. The tight junction protein ZO-1 establishes a link between the transmembrane protein occludin and the actin cytoskeleton. J Biol Chem. 1998;273(45):29745–53.
89. Panou DA, et al. Cell-penetrating peptides as carriers for transepithelial drug delivery. In: Langel Ü, editor., et al., Cell penetrating peptides. Cham: Springer; 2021.
90. Begum G, et al. Rapid assessment of ocular drug delivery in a novel ex vivo corneal model. Sci Rep. 2020;10(1):11754.
91. Ebrahim AS, et al. A novel combination therapy Tβ4/VIP protects against hyperglycemia-induced changes in human corneal epithelial cells. Biosensors. 2023;13(11):974.
92. Jian H-J, et al. Super-cationic carbon quantum dots synthesized from spermidine as an eye drop formulation for topical treatment of bacterial keratitis. ACS Nano. 2017;11(7):6703–16.
93. Boddu S, Gupta H, Patel S. Drug delivery to the back of the eye following topical administration: an update on research and patenting activity. Rec Pat Drug Deliv Formul. 2014;8(1):27–36.

Publisher's Note